nature communications

Article

https://doi.org/10.1038/s41467-025-64623-4

Nanomaterial signatures program biomolecular condensates via triphasic separation for chemoplasticity remodeling

Received: 22 April 2025

Accepted: 23 September 2025

Published online: 29 October 2025

Check for updates

Liu-Ting Zheng[1,5], Zeng-Shuai Yan[2,5], Xin-Yue Li[1,5], Jia-Jia Chang[1], Xiao-Qi Tan[1], Yu-Xing Wang[1], Hong-Ming Ding[2] ✉, Qin Liu[3] ✉, Yu-Qiang Ma[4] ✉ & Da Huo[1] ✉

Membraneless organelles form by phase separation and regulate cell behavior. We show that cholesterol-patterned AuNPs program nanomaterial-induced stress granules (NSGs) by lowering G3BP1 condensation barriers through a solid–liquid–liquid triphasic sequence: nanomaterials recruit hnRNPC, which then engages G3BP1 to nucleate gel-like condensates. We map NSG microenvironments (temperature, polarity, pH, and proteasome activity), uncover dual disassembly—a slow VCP/19S-dependent route and a rapid SUMO/20S-dependent backup—and show that NSGs remodel chemo-plasticity: they mitigate doxorubicin/cisplatin toxicity in normal tissues yet sensitize tumors to nocodazole in vivo. Local induction and selective dissolution of NSGs thus offers a strategy to decouple efficacy from toxicity. Our results establish design rules linking nanomaterial surface chemistry to condensate programming and provide actionable levers to steer therapeutic outcomes.

Membrane-less organelles (MLOs) are dynamic cellular structures formed through liquid-liquid phase separation (LLPS) of scaffold proteins and RNAs, playing critical roles in various biological processes[1]. Stress granules (SGs), a typical example of MLOs, emerge in eukaryotic cells subjected to stimulation, including oxidative stress, heat-shock, or hyperosmotic treatment[2,3]. Under such conditions, the translational activity of mRNA is temporally halted. By taking RNA-binding protein bound to mRNA as the core, followed by the recruitment of client proteins, SGs can be established that serve a pro-survival role[3,4]. Among the various types of SGs that differ in origination, G3BP1 is ubiquitous that functions as the central hub owing to its intrinsic interaction with RNA as mediated by the RNA-recognition motif[5]. In responding to stress relief, SGs undergo programmed disassembly to unleash sequestered mRNAs for resuming translation[6]. As such, the formation of SGs offers the stressed cells a means to temporarily control the energy consumption to balance the damage repair and homeostasis processes.

Emerging evidence indicates a correlation between SGs and the chemo-plasticity of cells[7–9]. When exposed to chemotherapeutics such as cisplatin, wild-type cancer cells that extensively express SGs demonstrate a significantly higher survival rate compared to their counterparts lacking G3BP1[10]. The modulation of chemo-plasticity by SGs can primarily be attributed to the sequestration of pro-apoptotic components within the organelle[11]. Due to their metastable nature, the influence of SGs on chemo-plasticity can be transient and temporally regulated[8,12], presenting unique advantages over conventional chemotherapy and identifying MLOs as promising targets for cancer treatment. However, several limitations need to be addressed to achieve this goal. Firstly, the complex structure of SGs requires drugs capable of simultaneously interfering with multiple proteins, which is

[1]School of Pharmacy, Department of Pharmaceutics, Nanjing Medical University, Nanjing, Jiangsu, China. [2]Center for Soft Condensed Matter Physics and Interdisciplinary Research, School of Physical Science and Technology, Soochow University, Suzhou, Jiangsu, China. [3]Department of Oncology, Nanjing Drum Tower Hospital, Affiliated Hospital of Medical School, Nanjing University, Nanjing, Jiangsu, China. [4]National Laboratory of Solid State Microstructures and Department of Physics, Collaborative Innovation Center of Advanced Microstructures, Nanjing University, Nanjing, Jiangsu, China. [5]These authors contributed equally: Liu-Ting Zheng, Zeng-Shuai Yan, Xin-Yue Li. ✉e-mail: dinghm@suda.edu.cn; liuqin@nju.edu.cn; myqiang@nju.edu.cn; huoda@njmu.edu.cn

beyond the capability of most small molecules[13]. Additionally, despite the varied origins of different SG subtypes, their contribution to mitigating chemo-toxicity is relatively consistent, and the presence of pro-apoptotic counterparts remains unclear, which is critical for tumor eradication. Furthermore, therapies aimed at modulating SGs must possess spatial precision to confine their influence to specific tissues, thereby mitigating global side effects. Meeting these criteria is essential for the successful development of therapeutics targeting the SGs-chemo-plasticity axis, which remains technically challenging.

The advancement of multifunctional and integrated therapeutic systems through nanotechnology represents a potential approach to address these challenges. Gold nanoparticles (AuNPs) are considered useful platforms in cancer therapy due to their biocompatibility, ease of surface functionalization, and superior stability[14,15]. Although current research has observed passive interactions of nanomaterials with G3BP1 and other stress-related counterparts, the ability of rationally designed nano-platforms to remodel SGs remains unclear. While some evidence suggests that the physicochemical features of AuNPs significantly influence nanomaterials-protein interplay[16], yet there lacks a comprehensive study revealing how these signatures impact the interaction between nanomaterials and SGs.

In this study, we constructed a library of AuNPs with varying signatures in terms of surface charge and hydrophobicity. Utilizing chemo-etching-assisted proximity labeling and immunofluorescence techniques, we systematically decoded the network of adsorbed proteins in an unbiased manner and examined their correlation with the surface functionalization features of AuNPs. Surprisingly, among the various candidates, a platform partially enclosed by a cholesterol (CLS)-terminated ligand demonstrated the ability to establish SGs through heterogeneous growth by serving as the seeds. Regarding the unprecedented establishment of SGs in a stress-free manner, we next employed computational simulation to assess the underlying mechanisms. We proposed and validated through truncation assays and proximity assessment that a stepwise phase separation occurs via sequential recruitment of hnRNPC and G3BP1 by CLS-ligand. Considering the physical properties of nanomaterials and adsorbed proteins, this process was termed “solid-liquid-liquid” tri-phase separation, ultimately leading to the formation of non-canonical SGs (c-SGs), namely, nanomaterials-induced SGs (NSGs). Unlike c-SGs, NSGs exhibit a gel-like structure that hinders component exchange with diluted phases, confirmed by the photo-bleach recovery assay. Given this unique feature, the dissociation pathway of NSGs is expected to differ from that of c-SGs, further explored using inhibition assays and transcriptome analysis. The disassembly of NSGs revealed an unprecedented dual-mode pathway dominated by a slow yet robust 19S proteasome-dependent mechanism alongside a 20S-dependent backup pathway functioning upon inactivation of the former. Formation of NSGs was validated to be capable of reshaping the chemo-plasticity of cells, thereby leading to context-dependent therapeutic outcome remodeling. Through spatially controlled introduction of CLS-functionalized AuNPs as the inducer of NSGs, we investigated a set of ideas, including in vivo chemo-toxicity mitigation and sensitization in normal and cancerous tissues, respectively. The role of NSGs in these processes was further validated using mice with liver and tumor tissue, conditional knockout of pivotal NSGs genes. A schematic illustration provided in Fig. 1 summarizes the core concepts and findings of the study, offering insight into the role of NSGs in nanomaterials metabolism and shedding light on the development of artificial, functional MLO for precision disease management.

Results

Nanomaterials signature-regulated SGs

In this study, we synthesized a library of gold nanoparticles (AuNPs) with varying sizes from 10 nm to 180 nm (refer to Fig. 2A), employing seed-mediated growth[17]. The size of the synthesized AuNPs was characterized using transmission electron microscopy (refer to Supplementary Fig. 1). To investigate the interaction between these nanoparticles and stress granule-associated proteins, we analyzed the impact of differently sized AuNPs on the condensation of G3BP1 protein within HeLa cells. Notably, an inverse correlation was found between the extent of G3BP1 condensation and the size of the AuNPs (refer to Fig. 2B). Based on these observations, we selected AuNPs with a diameter of 70 nm due to their minimal influence on G3BP1 condensation, thereby reducing the confounding effects of nanomaterial size. In subsequent discussions, unless otherwise specified, AuNPs refer to 70-nm gold nanoparticles.

We functionalized AuNPs with polyethylene glycol (PEG) of different molecular weights, as shown in Fig. 2A, and characterized their optical features using UV-vis spectra (Supplementary Fig. 2). We then examined how PEG chain length affected the cellular uptake of AuNPs by HeLa cells and G3BP1 condensation. Longer PEG chains reduced both G3BP1 condensation and AuNP endocytosis (Supplementary Fig. 3). For a balanced performance, we fixed PEG molecular weight at 5 kDa for further analysis. Next, we investigated the role of AuNP surface charge and hydrophilicity in regulating G3BP1 condensation. We used NH_2-/COOH-/OMe-PEG-SH and mixtures of CLS-PEG-SH and mPEG-SH at varying ratios (20%-100%) to study these effects. Specifically, NH_2-modified and 60% CLS-AuNPs significantly stimulated SGs formation (Supplementary Fig. 4, 4.37 and 3.05-fold, respectively, compared to control) and showed 68.5% colocalization with the MLOs (Fig. 2C-E), the highest among all groups. Positively charged materials, like those rendered by the NH_2 group, can either stimulate stress response due to intrinsic toxicity (for instance, gold nanorods[14]) or provoke SGs by acting as RNA-binding proteins that aid the G3BP1 assembly[4,16]. The mechanism for CLS-modified nanomaterials, excluding the likelihood of seeding SGs through electrostatic interaction, is yet to be defined.

To ascertain if phase separation induced by 60% CLS-AuNPs is a universal phenomenon, we extended our assay to other LLPS-prone proteins such as YTHDF2, TDP43, and SIRT2, using $NaAsO_2$ (AS) as a classic inducer. We observed that 60% CLS-AuNPs significantly reduced the phase-separation energy barriers for G3BP1 and YTHDF2 proteins in cells (Supplementary Fig. 5A, showing reductions of 1.74-, 1.44-, and 1.47-fold for G3BP1 and 1.08-, 1.01-, and 1.24-fold for YTHDF2 at 15 min, 30 min, and 60 min post-treatment, respectively, relative to AS-treated control groups). As an essential component of SGs, YTHDF2 can form droplets that closely overlap with SGs through coacervation[18,19], which explains the ability of nanomaterials to stimulate YTHDF2 puncta. Given the difference in size between SGs induced by nanomaterials and canonical SGs stimulated by AS, the former were termed NSGs. Conversely, the condensation of SIRT2 and TDP43—proteins forming MLOs only weakly associated with SGs[20]—was unaffected by 60% CLS-AuNPs (Supplementary Fig. 5A). These findings indicate that 60% CLS-AuNPs preferentially target components associated with SGs.

A common outcome of nanomaterials’ exposure to biological media such as serum is the protein corona effect, where proteins rapidly cover the surface of nano-substances. It is unclear whether proteins adsorbed prior to cellular entry of 60% CLS-AuNPs are involved in nanomaterials-G3BP1 interactions. A simplified assay was conducted to examine the biodistribution of the protein corona after endocytosis. To distinguish extracellular from intracellular proteins, serum proteins conjugated with a click-handle were prepared for cell culture and subsequent formation of the protein corona, as shown in Supplementary Fig. 5B. Tetrazine-expressing proteins—either remaining on nanomaterials (Component I) or detached (Component II)—were isolated using a click-reaction and magnetic beads. Albumin, as the predominant component, was used as a reference for expression analysis in both components (Supplementary Fig. 5C). A significant reduction in protein corona was observed for 60% CLS-AuNPs,

https://doi.org/10.1038/s41467-025-64623-4

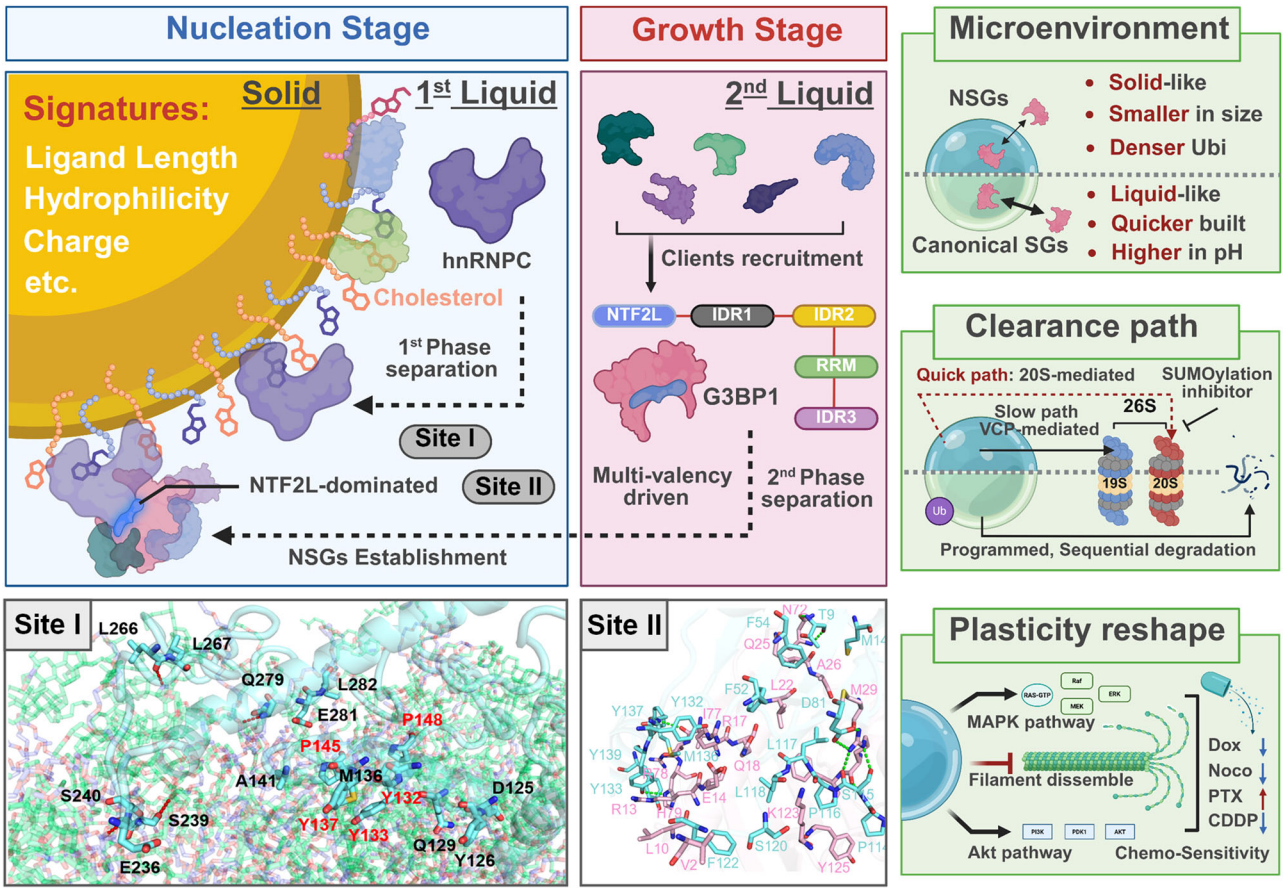

Fig. 1 | Formation mechanism and key features of NSGs. The formation of nanomaterial-induced stress granules (NSGs) is characterized by an initial nucleation stage involving the specific adsorption of hnRNPC (Site I: solid and 1st liquid phase separation), followed by a growth stage that entails the recruitment of G3BP1 by the former as mediated by the NTF2L domain of the latter (Site II: 1st liquid-2nd liquid phase separation). In contrast to canonical SGs, NSGs feature a substantially different physicochemical microenvironment as well as clearance path, which collectively contribute to their function as a remodeling hub for chemo-plasticity. Created in BioRender. Huo (2025) https://BioRender.com/d1k9zmc.

consistent with previous reports indicating different fates for protein corona and nanomaterials involving cycling endosomes[21]. Although the precise mechanism behind the disassembly of the protein corona in this context has not been determined, current findings suggest that previously adsorbed proteins did not play a key role in the nanomaterials-G3BP1 interaction.

Mechanism of NSG formation

Endoplasmic reticulum stress (ER-stress) frequently occurs and serves as an early event stimulating the formation of SGs[22]. We first examined the presence of ER-stress in cells exposed to 60% CLS-AuNPs, indicated by the expression level of CHOP and BiP (Fig. 2F). The absence of ER-stress ruled out the possibility of 60% CLS-AuNPs stimulating NSG through a classic mechanism involving misfolded protein accumulation[23]. Next, potential pathways underlying the action of 60% CLS-AuNPs were screened using RNA-sequencing. Cells exposed to 40 kDa mPEG modified AuNPs were used as a negative control, wherein the absence of noticeable NSGs was confirmed. Thus, altered genes (compared to untreated cells) in the mPEG group can be identified as irrelevant to NSGs assembly, reflecting the cellular response to the nanomaterial itself, rather than the signature. Gene Ontology (GO) analysis and Kyoto Encyclopedia of Genes and Genomes (KEGG) enrichment analysis were conducted with a focus on significantly altered genes that only appeared in the CLS group. Results showed no candidates had a clarified interplay with SGs (Fig. 2G), suggesting that the induction of NSGs proceeds independently of transcriptional level changes.

Considering the tendency of nanomaterials to recruit proteins, especially those with intrinsically disordered regions, we hypothesize that variations in the nanomaterial signature can affect the preference of recruited proteins as well as their conformation, thereby impacting SGs assembly. To thoroughly identify the adsorbed proteins, we developed a chemo-etching-assisted proximity labeling method to capture the fragile adsorbed complex on the nanomaterial surfaces, as illustrated in Fig. 2H, alongside co-immunoprecipitation (Co-IP) techniques to uncover the proteins associated with G3BP1. Analysis of surface-adsorbed proteins revealed that NSGs formed in response to 60% CLS-AuNPs stimulation differ compositionally from canonical SGs induced by AS (Fig. 3A). Notably, NSGs contained a higher proportion of proteins associated with translation processes, including ribosomes and rRNA binding factors. This observation suggests that NSGs might have the capacity to induce transient cell cycle arrest and preserve ATP by recruiting translation-associated components, thus exerting a pro-survival role in stressed cells.

Subsequently, we compared the proteins adsorbed on the nanomaterial surfaces—captured via photo-proximity labeling—with those that interact closely with G3BP1 in NH_2- and 60% CLS-AuNPs groups. Among the common proteins identified, we observed that nine proteins within the 60% CLS-AuNPs group exhibit potential association with G3BP1 (Fig. 3B). The ability of these components to undergo LLPS was further assessed based on the proportion of disordered regions and physicochemical properties of each protein using PhaSePred[24]. The calculated scores are as follows: hnRNPU (0.947), SYNCRIP (0.945), hnRNPC (0.920), DHX9 (0.917), hnRNPK (0.914), HSPA9

https://doi.org/10.1038/s41467-025-64623-4

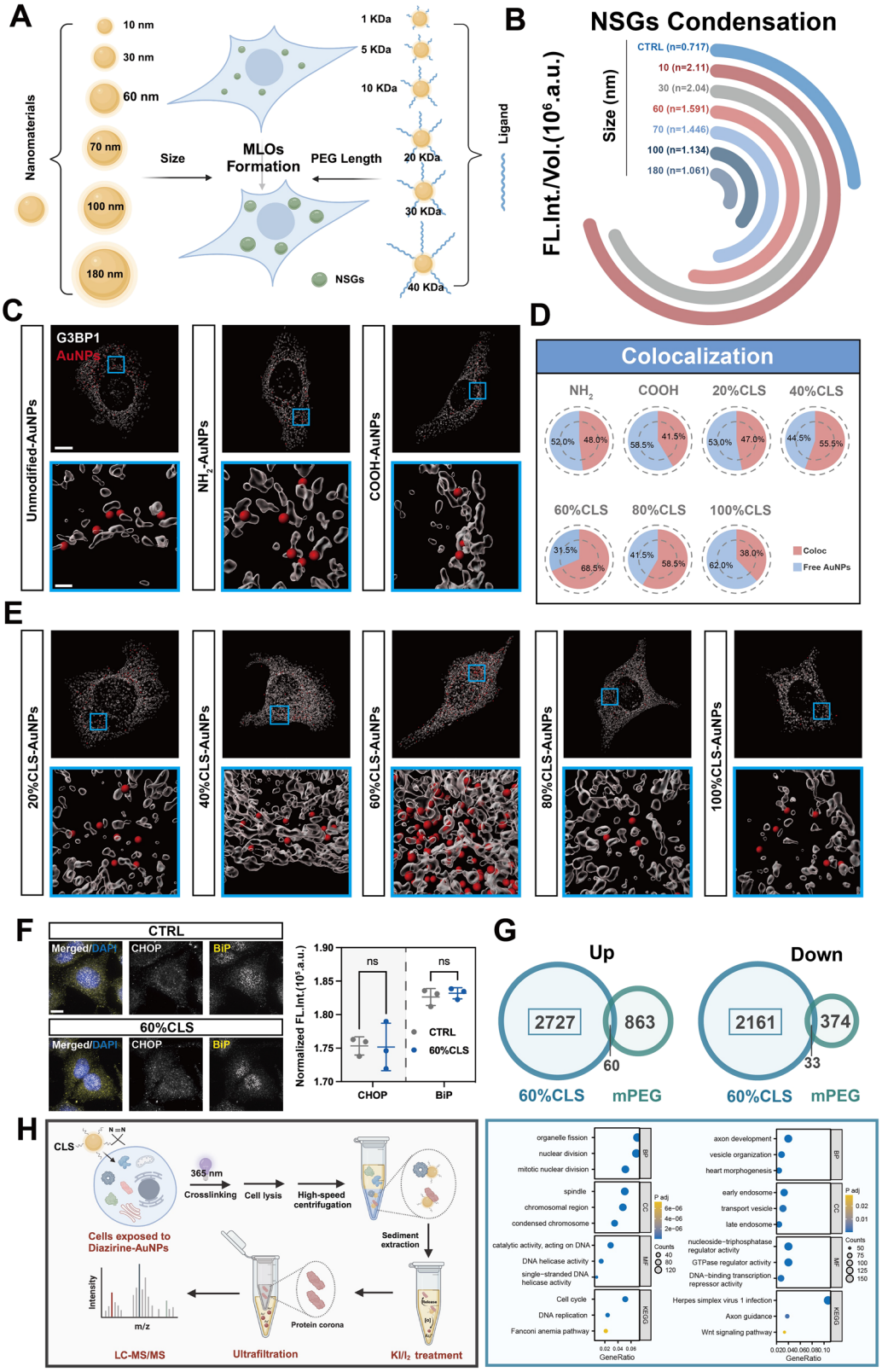

(0.793), PTBP1 (0.612), ACTB (0.498), and FN1 (0.166). Conversely, only three proteins from the NH_2-group interacted with G3BP1, yielding an average phase separation score of 0.677, which is significantly lower than that of the CLS group (0.746), aligning with their differences in nanomaterials-NSGs colocalization efficiency. We propose that the enhanced phase separation potential of the proteins found in the CLS group may contribute to their increased capability to seed NSGs compared to NH_2-modified materials.

Combining the interaction components of G3BP1 in both experimental groups, we observed the presence of hnRNPC (Fig. 3B). Previous analyses indicated that mPEG-functionalized AuNPs could induce NSGs, albeit to a lesser extent than CLS- or NH_2-modified

Fig. 2 | Suitably functionalized nanomaterials stimulate NSGs. A Schematic illustrates the nanomaterial library evolved for MLOs-induction. Created in BioRender. Huo (2025) https://BioRender.com/9nqrrs7. **B** A circular strip chart elucidates the extent of G3BP1 condensation extent induced by nanomaterials ($n \geq 200$ G3BP1 puncta per group from 3 independent biological replicates). Fluorescence graphs displaying the colocalization of (**C**) surface charge and (**E**) hydrophilicity-differed AuNPs with SGs ($n = 3$ independent biological replicates). Cells received pristine AuNPs serve as a control group for comparison. In reconstructed graphs (shown beneath each fluorescence data), AuNPs were shown as red spots with SGs displayed in their transparent form to ease the visualization. Scale bars: 10 μm and 1 μm for graphs of low-magnification and zoomed region (highlighted with a square), respectively. **D** Corresponding colocalization efficacy between SGs and nanomaterials ($n \geq 200$ cells per group, biological triplicates). **F** Immunofluorescence graphs of ER-stress biomarker expression in cells receiving 60% CLS-AuNPs. Control (CTRL) here stands for untreated cells. The normalized fluorescence intensity (FL.Int, arbitrary units: a.u.) of proteins was plotted on the right. The data represent mean ± SD calculated ($n = 3$ independent biological replicates). ns indicates $p > 0.05$. **G** Venn diagram of differentially expressed genes (DEGs) in 60%CLS- and mPEG- groups with respect to untreated cells as the control. Significant changes are indicated by a fold change of either higher than 2 (up-regulated) or lower than 0.5 (down-regulated). Bioinformatic analysis of enriched pathways for both up- and down-regulated genes in certain groups was presented below. Color-coding of points stands for their adjusted *p*-value and gene counts. **H** A schematic illustrating the working flow of chemo-etching-assisted proximity labeling. For more details, please refer to the Methods section. Created in BioRender. Huo (2025) https://BioRender.com/n369p5k. Source data are provided as a Source Data file.

counterparts. We extended the photo-proximity labeling to the mPEG group, alongside co-IP assays to elucidate the interactome between nanomaterials and G3BP1, respectively (referred to as material and G3BP1 side in Fig. 3C). Venn diagram analysis revealed hnRNPC as the only overlapping component linking NSGs derived from different origins and nanomaterials, showcasing its capacity to undergo LLPS by serving as clients (Fig. 3D).

We subsequently examined the role of hnRNPC in establishing NSGs. Given the bi-directional interaction of hnRNPC with G3BP1 and nanomaterials, we performed a competition assay to evaluate hnRNPC's preference towards NSGs *versus* canonical SGs (denoted as f-SGs). As shown in Fig. 3E, simultaneous exposure to 60% CLS-AuNPs and AS resulted in the co-existence of NSGs and f-SGs, distinguishable based on their colocalization with dye-labeled nanomaterials. A stronger association between hnRNPC and nanomaterials compared to G3BP1 was confirmed by the higher protein abundance in NSGs (Figs. 3F, 1.29-fold of f-SGs, $p < 0.05$). Furthermore, colocalization analysis demonstrated that the introduction of either CLS-AuNPs or AS treatment promoted a stronger association between G3BP1 and hnRNPC (Fig. 3G). Notably, the co-presence of NSGs and f-SGs (60% CLS + AS group) further strengthened the interaction between these two components compared to AS treatment alone. This observation confirmed that within NSGs, hnRNPC interacts more intimately with G3BP1 compared to f-SGs.

In stressed cells, regardless of the type of stimuli, we observed the aberrant translocation of hnRNPC from the nucleus to the cytoplasm, consistent with its role as a client that promotes the formation of SGs (Fig. 3H, I). Notably, the presence of nanomaterials further enhances the cytoplasmic entry of hnRNPC compared to G3BP1 condensation alone (AS group). We hypothesize that the recruitment of hnRNPC by nanomaterials may be a critical event promoting the establishment of NSGs. To test this hypothesis, we performed the same assay in cells lacking *hnRNPC* (*hnRNPC* KO, Fig. 3K). The absence of hnRNPC did not affect AS's ability to induce SGs, likely due to the presence of multiple alternative clients (Fig. 3L). In contrast, *hnRNPC* KO significantly reduced the capacity of nanomaterials to provoke NSGs, with G3BP1 condensation decreased by 1.38-fold (Fig. 3L). These results clearly demonstrate the role of hnRNPC in facilitating NSG formation. Collectively, our findings suggest a model of NSG formation wherein the translocation of hnRNPC from the nucleus to the surface of CLS-modified nanomaterials initiates the recruitment of G3BP1, thereby driving NSG assembly (Fig. 3M).

An additional question is how the formation of NSGs affects the cellular capacity to form canonical SGs and their interaction. To investigate this, cells were simultaneously exposed to 60% CLS nanomaterials and canonical SG inducers (AS, sorbitol, and heat-shock). As shown in Supplementary Fig. 6A, this co-exposure resulted in the concurrent formation of both NSGs and canonical SGs in all tested conditions, indicating that NSG formation minimally impacts the G3BP1 pool. The experiment was then modified so that exposure to canonical SG inducers occurred after nanomaterial stimulation. It was observed that prior NSG generation substantially reduced the ability of cells to form canonical SGs (Supplementary Fig. 6B). Previous findings have established that hnRNPC plays a key role in mediating interactions between nanomaterials and G3BP1, making nanomaterials a less competitive substrate for G3BP1 phase separation compared to conventional stressors. Therefore, simultaneous exposure did not significantly reduce the cells' ability to form canonical SGs. In contrast, sequential exposure enabled nanomaterials to recruit G3BP1 more effectively, leading to depletion of the protein pool and a diminished ability of cells to form canonical SGs.

Molecular dynamics simulations of tri-phase separation

To generate the mechanistic hypothesis, we employed all-atom MD simulations to explore the sequential recruitment of hnRNPC and G3BP1 to AuNPs, where 500 ns production simulations were performed following pre-equilibration, and the final 200 ns, corresponding to the equilibrium phase, were used for subsequent analyses (details described in the Methods section). Compared to mPEG, the incorporation of 60% CLS-PEG results in the formation of larger patches on the outer surface of AuNPs due to strong hydrophobic interactions among CLS molecules (Supplementary Fig. 7A–C). These hydrophobic interactions reduce the conformational flexibility of CLS-PEG and extend the residence time of water molecules on the PEG surfaces (Supplementary Fig. 7D–F), thus altering local hydrophilicity. Notably, the surface undulations of 60% CLS resulted in a surface area of 252.98 nm^2, which is significantly higher than that of the other two groups (163.23 nm^2 and 184.80 nm^2 for mPEG and 100% CLS, respectively) (Supplementary Fig. 7G). These features collectively suggest that 60% CLS-AuNPs exhibit distinct adsorption behaviors when interacting with hnRNPC.

Subsequently, we simulated the interaction between hnRNPC and nanomaterials, placing hnRNPC on top of three different types of AuNPs. Successful adsorption was confirmed across all tested groups with negligible differences (Fig. 4A–I and Supplementary Figs. 8 and 9); however, the binding strength and interfaces varied significantly (Fig. 4J, K). Specifically, a much closer interaction between hnRNPC and 60% CLS-AuNPs was observed compared to the other two groups in terms of contact surface area (CSA: 46.22, 30.41, and 41.47 nm^2 for 60%-CLS, 100%-CLS, and mPEG, respectively) and binding energy (−421.38, −197.98, and −319.08 kcal/mol). These differences were further supported by the greater number of residues at the hnRNPC-nanomaterial interface compared to the other two groups (Fig. 4M–O). Specifically, N-terminal residues of hnRNPC, including K8, T9, D10, P11, R12, M14, K42, R61, and P88 (Fig. 4N), predominantly contributed to the recruitment of hnRNPC to 60% CLS-AuNPs. Additionally, interactions between hydrophobic residues (P145, P148, Y132, Y133, and Y137) and CLS at the hnRNPC-60% CLS-AuNP interface facilitated hnRNPC adsorption (Fig. 4D). In contrast, the total or partial absence of similar interactions or compensatory forces in fully cholesterolized (100% CLS

https://doi.org/10.1038/s41467-025-64623-4

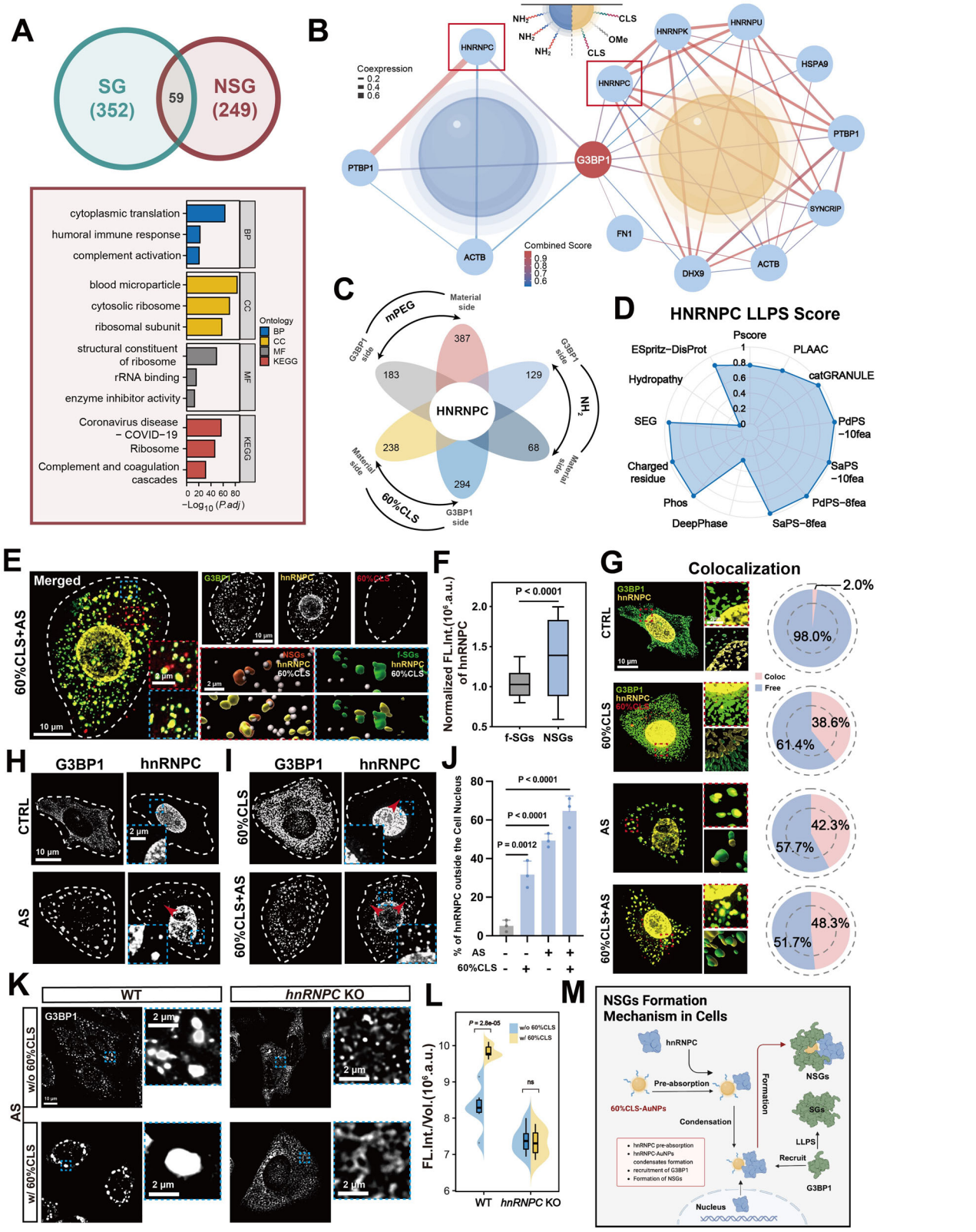

group) or cholesterol-devoid (mPEG group) groups safely explained the weakened adsorption performance of hnRNPC.

We further investigated the interaction between hnRNPC, stabilized by nanomaterials, and G3BP1. Using ClusPro[25] and AlphaFold3[26], we predicted the complex structure to identify the binding region between the NTF2L domain of G3BP1 and hnRNPC. The structures obtained from both approaches are nearly identical (Supplementary Fig. 10A), demonstrating that the binding of the NTF2L pocket with $Coil_{111\text{-}123}$ residues of hnRNPC is critical for recruitment. To confirm the stability of the complex structure, energy minimization, a short pre-equilibration in NVT and NPT ensembles, and final 500 ns production simulations were conducted. The NTF2L-hnRNPC binding energy was calculated over the equilibrated final 200 ns, indicating a stable complex with a binding energy of −258.24 kcal/mol (Supplementary

Fig. 3 | Mechanisms of NSG assembly driven by hnRNPC recruitment. A Venn diagram of proteins associated with canonical SGs and NSGs, with corresponding gene ontology analysis of unique components in the NSGs group shown below. **B** Protein-protein interaction (PPI) network elucidating the key components that interact with G3BP1 in NH_2 and 60% CLS groups. Created in BioRender. Huo (2025) https://BioRender.com/0k8dayr. **C** The petal Venn diagram identifies the ubiquitous protein hnRNPC critical for NSGs formation. **D** Radar chart shows the LLPS capacity of hnRNPC. **E** Immunofluorescence graphs showing the colocalization of hnRNPC with NSGs and free SGs (denoted by f-SGs). 3D-reconstructed information can be found beneath the fluorescence graphs, with certain components pseudo-colored as noted. Normalized fluorescent intensity (FL.Int.) of hnRNPC in f-SGs and NSGs was quantified as presented in (**F**, $n > 100$ hnRNPC puncta per group from 3 independent biological replicates, arbitrary units: a.u.). **G** Colocalization efficacy of G3BP1 and hnRNPC in origination-differentiated SGs ($n \geq 200$ cells per group, biological triplicates). For the color-coding, please refer to (**E**). Randomly depicted regions (marked by a red dashed square) were enlarged (upper panel in the middle) and reconstructed in 3D (lower panel in the middle). The percentage of colocalization is plotted in a pie chart on the right. Legends of Coloc and Free stand for hnRNPC colocalized with or away from G3BP1, respectively. **H** and **I** Condensation of G3BP1 and cytoplasmic translocation extent of hnRNPC upon exposure to 60% CLS-AuNPs, AS, and their combination. The proportion of outer nucleus hnRNPC can be found in (**J**). **K** Expression of SGs in wild-type and hnRNPC KO cells received stimulation of AS with (w/) or without (w/o) 60% CLS-AuNPs (60% CLS). Quantified condensation results (with fluorescence intensity of each droplet normalized by its volume) can be found in (**L**, arbitrary units: a.u.). **M** A schematic illustration revealing the proposed mechanism underlying the formation of NSGs, in which a tri-phase separation proceeded sequentially. Created in BioRender. Huo (2025) https://BioRender.com/jswqnld. Statistical differences were calculated using a two-tailed *t*-test or one-way ANOVA. Data represents mean ± SD (Independent biological replicates for J and L, 3 and 6, respectively). Source data are provided as a Source Data file.

Fig. 10B). Hydrophobic interactions mediated by residues in $Coil_{111\text{-}123}$, such as H111, P114, P116, L117, L118, and F122, play a key role in stabilizing the NTF2L-hnRNPC interaction (Fig. 5A, B). This attraction is similar to how the NTF2L domain recruits other G3BP1 clients, such as Caprin-1 or USP10, in the formation of stress granules[27].

After optimizing models describing the interaction of hnRNPC with either G3BP1 (NTF2L domain) or nanomaterials, a ternary complex including all these components was constructed (Fig. 5C, D). The presence of nanomaterials did not impair hnRNPC's ability to interact with the NTF2L domain of G3BP1, as indicated by the preservation of $Coil_{111\text{-}123}$ residues (such as P116, L117, L118, and F122) in the protein-protein interface (inset Fig. 5C). There might be contributions from other bystander proteins in stabilizing the hnRNPC-G3BP1 interaction, which are beyond the capacity of current simulation approaches to reveal. To validate the MD-informed hypothesis that hnRNPC interacts with G3BP1 through the NTF2L domain in cellular environments, an assay was conducted in cells overexpressing truncated G3BP1 (ΔNTF2L). As shown in Fig. 5E, super-resolution imaging was used to analyze the interaction of G3BP1 or its mutant with hnRNPC, measuring the distance between these proteins. The absence of the NTF2L domain significantly weakened the hnRNPC-G3BP1 interaction, as indicated by their enforced segregation (mean distance: 0.53 and 2.85 μm for control and ΔNTF2L groups, respectively). This finding confirmed the hypothesis of previous simulations and validated that the contribution of bystander components to the recruitment of G3BP1 is limited with respect to hnRNPC.

Combining the computational findings and experimental results, the formation mechanism of the nanomaterials-hnRNPC-G3BP1 ternary complex can be described as follows: The modification with CLS-PEG ligands at a density of 60% creates a microenvironment conducive to hnRNPC adsorption, involving both hydrophobic interactions and hydrogen bonds to varying extents. This step is crucial for the further recruitment of G3BP1, as the absence of hnRNPC prevented NSG assembly. Through multivalent interaction of the $Coil_{111\text{-}123}$ region on the hnRNPC side with the NTF2L domain of G3BP1, G3BP1 condensation around AuNPs is initiated, establishing NSGs. Unlike c-SGs that rely mainly on coacervation, NSG assembly is regulated through sequential client recruitment. In this scenario, hnRNPC (liquid phase) acts as the central hub linking nanomaterials (solid phase) and G3BP1 (liquid phase), shifting the LLPS of proteins from co-condensation to a cascade-like process. This mechanism is termed 'solid-liquid-liquid' tri-phase separation to describe the formation of NSGs.

Microenvironment of NSGs

Emerging evidence indicates that the formation of MLOs contributes to creating a metastable lumen in the cytosol, differing significantly between the condensed phase (intra-MLO) and dilute phase (inter-MLO)[11,28,29]. This characteristic allows cells to adjust metabolic activities dynamically without changing the entire cytoplasmic environment, balancing various reactions under subtly different conditions. Therefore, understanding the microenvironment of MLOs is essential for predicting their biological implications, which is the focus of this study.

We categorized the microenvironment of NSGs into physical and chemical classes, including temperature, polarity, pH, and proteasome activity. To analyze the local microenvironment of NSGs without affecting the overall cellular environment, we applied a biorthogonal approach using HaloTag labeling[30], as illustrated in Fig. 6A. Environment-responsive dyes were conjugated with a chloroalkane ligand recognized by Halo-protein fused to the C-terminal of G3BP1, resulting in dye immobilization within SGs and visualization of the physicochemical microenvironment.

For the physical microenvironment of NSGs, rhodamine B was chosen as the temperature reporter[31]. With increased temperature, energy consumption by rhodamine B via non-radiative dissipation is enhanced, reducing fluorescence intensity. Colocalization analysis (1D, Fig. 6B) supported the labeling conciseness between ligand-functionalized dye and NSGs. Compared to c-SGs stimulated by AS, the calculated fluorescence intensity of NSGs was higher than canonical counterparts (1.69-fold, Fig. 6F and Supplementary Fig. 11), indicating a lower internal temperature. Similarly, coumarin-343 dye estimated polarity[32], revealing high polarization in both NSGs and canonical ones (Fig. 6C). According to Ye and colleagues[33], polarized microenvironments facilitate macromolecule influx into certain biomolecular condensates, promoting secondary phase separation, consistent with NSG features established through multiple phase separations.

We proceeded to analyze the chemical properties of NSGs using Protonex- and LLVY-conjugated ligands, which respond to pH and proteasome variations, respectively. The Protonex dye exhibits increased fluorescence intensity with decreasing pH levels. Interestingly, as illustrated by the 1D fluorescence distribution plot (Fig. 6D), G3BP1 translocates from regions of high pH (canonical SGs) to areas of low pH (NSGs). This observation aligns with our previous proximity labeling results, indicating significant differences in the enrichment of proteins closely interacting with G3BP1 between NSGs and those stimulated by oxidative stress. Changes in proximal proteins correspond to expected variations in pH levels. Our subsequent investigations revealed that pH is not the only altered chemical feature of NSGs compared to c-SGs. Utilizing LLVY as a cleavable, fluorogenic substrate for evaluating proteasome activity, we observed that G3BP1 acts as the proteolytic center within NSGs (suggested by its perfect overlap with dye molecules) and the absence of similar findings in the AS group (Supplementary Fig. 12, 5.5‰ of NSGs). Proteasomes, being highly susceptible to damaged proteins, suggest an accumulation of misfolded components in NSGs. As these MLO-associated clients unfold,

https://doi.org/10.1038/s41467-025-64623-4

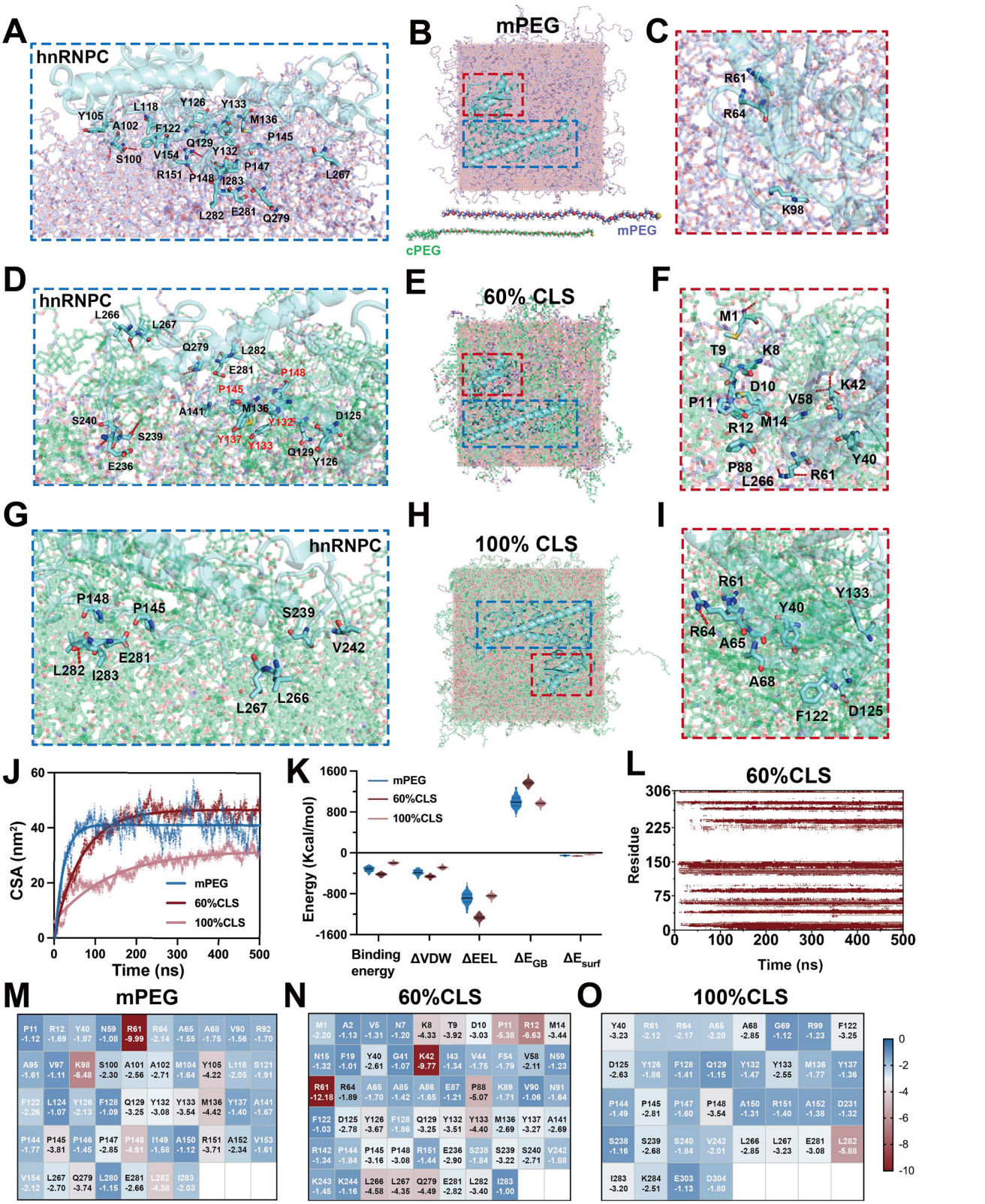

Fig. 4 | Simulated landscape for the adsorption of hnRNPC onto AuNPs. Representative snapshots revealing the binding conformation and contact interface of hnRNPC adsorbed onto (**A**–**C**) mPEG, (**D**–**F**) 60%CLS, and (**G**–**I**) 100%CLS. The red dashed lines represent hydrogen bonds. Enlarged view of marked regions (**B**, **E**, and **H**) can be found in (**A**, **D**, **G**, and **C**, **F**, **I**) based on the color-coding of dashed squares. **J** The contact surface area (CSA) and **K** interaction energies between hnRNPC and AuNPs (Data points were hidden from presentation to ease the visualization of median value; entire information can be found in source data). The central solid lines in panel K are the median, dashed lines stand for 25th and 75th percentiles, whiskers stand for 5th and 95th percentiles ($n = 3$ independent biological replicates). **L** Time evolution of the contact map between hnRNPC and the surface of 60% CLS-AuNPs. **M**–**O** Key residues of hnRNPC located in protein-AuNP interface that substantially contributed to their contact, defined as residues with a contribution greater than 1 kcal/mol. Source data are provided as a Source Data file.

https://doi.org/10.1038/s41467-025-64623-4

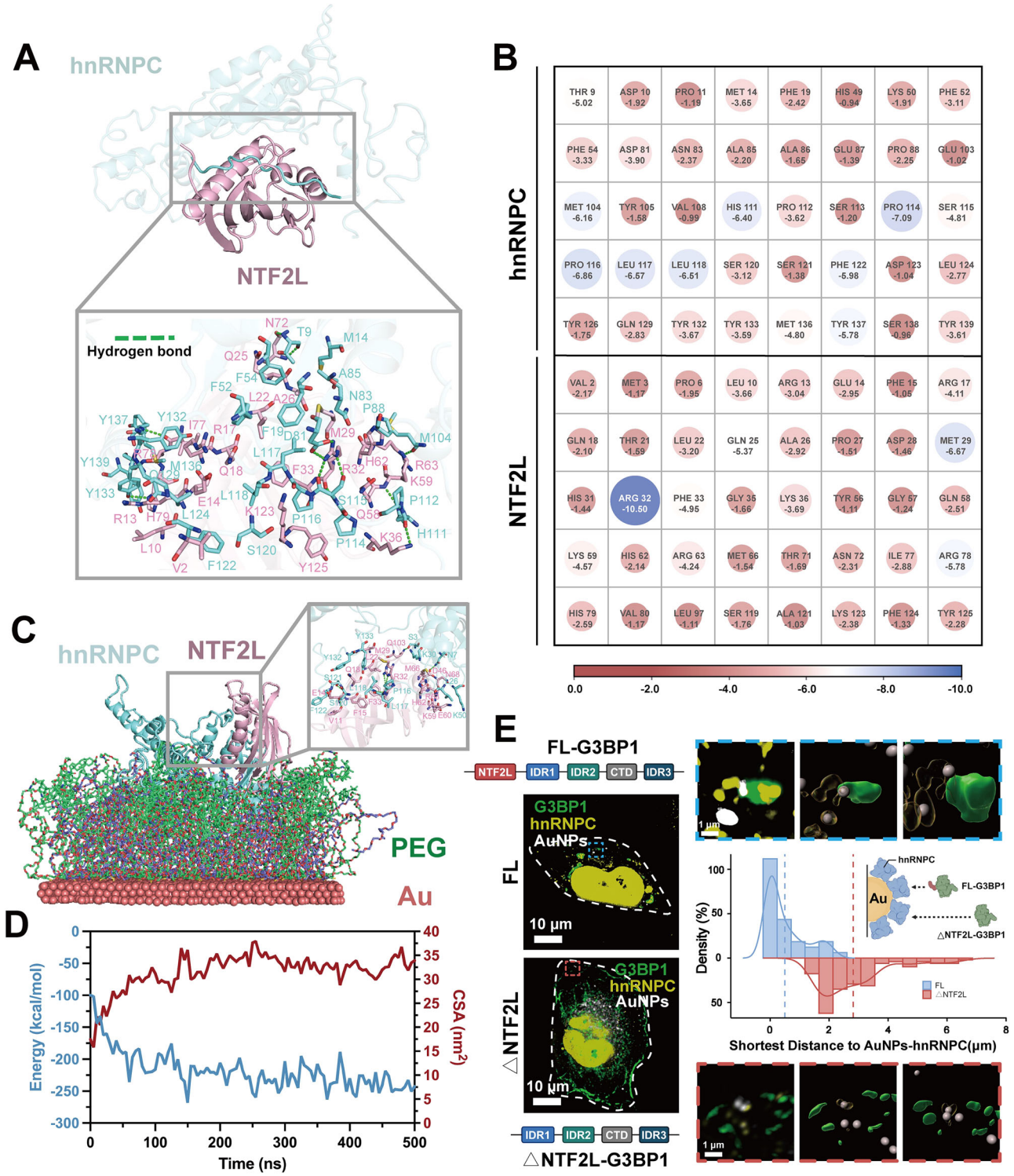

Fig. 5 | Mechanism underlying hnRNPC-G3BP1 interaction. A The binding conformation and contact interface of hnRNPC-NTF2L complex. **B** Key residues at the hnRNPC-NTF2L interface that make significant contributions to the binding energy (for its definition, please refer to Fig. 4M). **C** The conformation of the nanomaterial-hnRNPC-NTF2L ternary complex. **D** Time evolution of the interaction energy and CSA between NTF2L and the hnRNPC adsorbed on nanomaterials. **E** Immunofluorescence graphs of 60% CLS-AuNPs-treated cells overexpressing wild-type (FL) and truncated (ΔNTF2L) G3BP1 (both pseudo-colored in green) illustrate the susceptibility of G3BP1 towards the nanomaterial-hnRNPC complex. An enlarged view of the marked regions in each group (blue: FL; red: △NTF2L) was reconstructed in 3D as shown on the right side. The cell boundary was highlighted with white dashed lines for better visualization. The distance of G3BP1 to AuNPs-hnRNPC complex ($n \geq 30$ cells per group from 3 independent biological replicates) was measured and depicted by a frequency distribution histogram, with a summative schematic provided (inset). Created in BioRender. Huo (2025) https://BioRender.com/hyjh4im. Source data are provided as a Source Data file.

https://doi.org/10.1038/s41467-025-64623-4

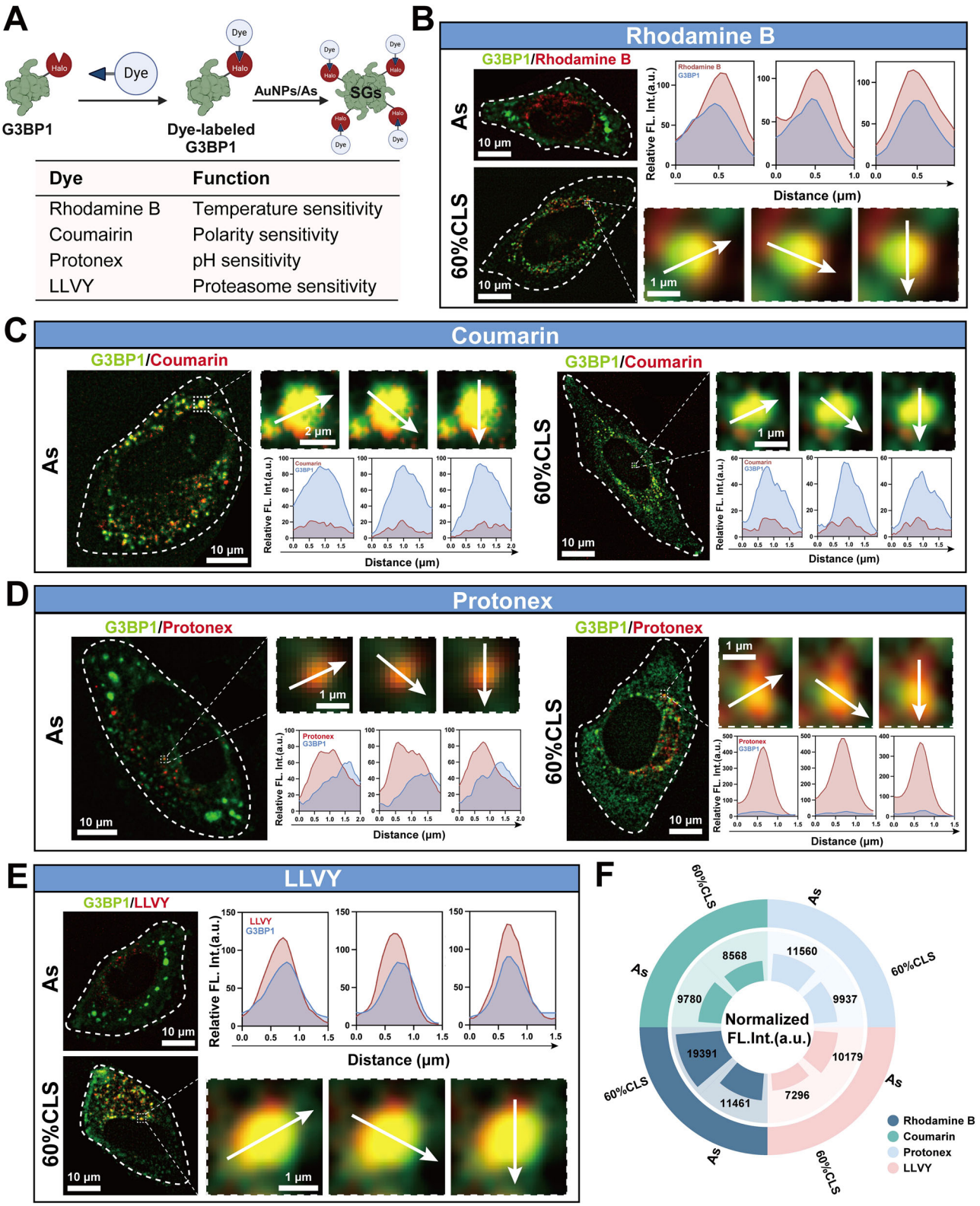

Dye	Function
Rhodamine B	Temperature sensitivity
Coumairin	Polarity sensitivity
Protonex	pH sensitivity
LLVY	Proteasome sensitivity

the packing of these components may intensify, leading to expected fluidity variation. To test this hypothesis, our subsequent analysis will focus on elucidating the physical properties of NSGs.

NSG dissociation mechanism

Enrichment of proteasomes suggests rigorous degradation occurring in certain regions, leading to a much-shortened half-life for NSGs. The timeframe assessment of NSGs revealed sustainable generation lasting for at least 8 h, followed by disassembly during the next 2 h, as indicated by the fold of changes in G3BP1 condensation extent measured at 2, 4, 6, 8, and 10 h (Supplementary Fig. 13: 1.57, 1.57, 1.84, 2.89, and 2.27-fold of control), whereas c-SGs typically undergo dissociation within 4 h post formation. As such, the stability of NSGs is unexpected and suggests concentrated proteasomes were either dysfunctional or acting in ways other than degradation machinery.

Fig. 6 | Characterization of the microenvironment in NSGs. A A schematic illustrating the methodologies employed for deciphering the SG microenvironment. Created in BioRender. Huo (2025) https://BioRender.com/bnyh25n. In this case, the HaloTag and fluorescence modality (GFP) are fused to G3BP1 at its C-terminal. Followed by the introduction of dye-conjugated Halo-ligand, a stable covalent bond can form between the ligand and HaloTag, thus allowing the visualization of SGs microenvironment. Representative fluorescence graphs, intensity profiles of cases involved (**B**) temperature-, (**C**) polarity-, (**D**) pH, and (**E**) proteolytic activity-sensitive dyes, respectively (arbitrary units: a.u.). GFP-tagged G3BP1 in cells receiving AS or 60%CLS-AuNPs was pseudo-colored in green. Cell membranes were outlined to guide the eye. The arrow delineates the direction associated with the quantification of fluorescence. For detailed information regarding the quantification of AS-stimulated SGs in Rhodamine B and LLVY, please refer to Supplementary Figs. 11 and 12. Shading underneath the curve was supplemented to ease the comparison with no additional scientific implication. Quantitative information based on the normalized fluorescence intensity of the four dyes is plotted in (**F**). Data represents mean ± SD (**B**–**E**, $n = 3$ independent biological replicates). Source data are provided as a Source Data file.

Our previous study indicated SGs provoked by nanomaterials might feature reduced fluidity compared to canonical ones stimulated by AS or heat stress[16]. It is unknown whether different nanomaterials exhibit similar implications. A comparative analysis of the physical features of NSGs and SGs elicited by canonical inducers (AS and sorbitol) was conducted using fluorescence recovery after photobleaching (FRAP) assays. Figure 7A shows the fluorescence recovery ratio of NSGs progressively reduced with extended durations of stimulation by 60% CLS-AuNPs (maximum recovery ratio: 85.5%, 64.7%, 40.6%, and 21.5% for AS, sorbitol, and treatments at 1 and 4 h with 60% CLS-AuNPs, respectively). This supports the notion that incorporation of CLS-AuNPs contributes to incremental solidification of NSGs, partially explaining the decreased degradative power of enriched proteasomes due to restricted traffic in solidified organelles.

We categorized the generated SGs in cells stressed with CLS-AuNPs into two groups: NSGs and those without nanomaterials' involvement (f-SGs). We repeated the FRAP assay on these groups to assess differences in fluidity. Under identical conditions, NSGs had a significantly lower recovery ratio compared to f-SGs (Fig. 7B, C, recovery values: 58.8% for f-SGs and 23.7% for NSGs). The preservation of liquid-like properties in f-SGs ruled out a global change in fluidity due to nanomaterial exposure, indicating a local effect in NSGs. Dissolution of MLOs can occur through programmed dissolution within the droplet, which is not possible when exchange between dense and diluted phases is prohibited[34,35], as seen in NSGs. Therefore, a dissociation mechanism differing from its liquid-like counterparts was expected for NSGs.

To understand NSGs degradation, we tested several inhibitors linked to SGs disassembly and nanomaterials-induced counterparts, including myricetin (HSP70 inhibitor), ML346 (HSP70 agonist), Grp94 (HSP90 inhibitor), AMP-PCP (HSP90 agonist), and CB5083 (VCP-p97 inhibitor). After confirming that these inhibitors do not induce SG formation alone (Supplementary Fig. 14A), we co-stimulated them with nanomaterials. Notably, VCP inhibitors notably accelerated NSG degradation (Supplementary Fig. 14B), showing the importance of the 19S proteasome in NSG maintenance. Similar results in HeLa$^{G3BP1\,OE}$ cells suggest the anti-degradation role VCP served is dispensable of G3BP1 abundance (Fig. 7D). Tests with other VCP-p97 inhibitors (DBeQ and NMS-859, Fig. 7E, F) supported these findings. As part of the 19S proteasome, VCP is known for degrading heat stress-induced SGs via ubiquitinated G3BP1, opposing our case[36]. It is thus hypothesized that alternative cytoplasmic degradation pathways might activate upon VCP-p97 inhibition. We next examined G3BP1 condensation under co-stimulation with 60% CLS-AuNPs and deubiquitinating enzyme inhibitor Spautin-1 or E1-activating enzyme inhibitor TAK-243. Neither inhibitor alone caused significant G3BP1 condensation (Supplementary Fig. 15). Co-stimulation with TAK-243 preserved NSGs better (Fig. 7G), while Spautin-1 reduced NSG stability. These results indicate a negative correlation between NSG preservation and ubiquitination extent.

We investigated the ubiquitination level of G3BP1 when the VCP-p97 pathway was inhibited. Comparing the expression of ubiquitinated G3BP1 in NSGs with the overall cytoplasmic protein ubiquitination level before and after CB5083 treatment, we found decreased G3BP1 ubiquitination as NSGs appeared (Fig. 7H). During this time, NSG formation exceeded degradation. Inhibition of VCP increased ubiquitinated G3BP1 levels and caused NSGs to depolymerize, indicating an alternative ubiquitination-related degradation pathway activable upon VCP inhibition. Stable ubiquitination level of cytoplasmic protein suggests the influence of this alternative pathway was limited (Fig. 8A, B). Combined CB5083 and nanomaterials treatment accelerated G3BP1 clearance with respect to nanomaterials alone (Fig. 8C), revealing strong degradation power compared to the VCP-mediated pathway. Thus, it can be concluded that two mechanisms coexist for NSG degradation: the slower VCP-p97-dependent route and a rapid, alternative one activated upon VCP inhibition. RNA-sequencing showed increased mRNA levels related to 20S proteasome activity, especially PSMA, PSMB, and PSME post 19S inhibition (Fig. 8D). Ubiquitinated proteins can be degraded by a 19S-independent mechanism associated with SUMOylation and 20S proteasome activity, often removing unfolded or damaged proteins[37]. We validated the role of 20S proteasome by stabilizing NSGs under nanomaterial stimulation with PYR-41, an ubiquitination inhibitor (Fig. 8E, F, Supplementary Fig. 16). This stability was largely restored by introducing a SUMOylation inhibitor (2-D08), confirming the contribution of SUMOylation to NSG degradation. Under physiological conditions, the 19S-mediated route is the rate-limiting step, whereas the 20S-dominated degradation path, once inactive, can accelerate NSG clearance. Using proximity analysis, we validated the hypothesis of 20S proteasome-mediated degradation. We analyzed the interaction of PSMB6 (part of the 20S proteasome complex) with nanomaterials before and after inhibition of VCP. Suppressed VCP activity increased the interaction of G3BP1 with the 20S proteasome, as indicated by their reduced distance to each other (Fig. 8G), whereas the absence of nanomaterials abolished this effect. This suggests that the 20S proteasome functions as a backup degradation pathway exclusively for NSGs, which is inhibited by 19S counterparts under normal conditions.

We also investigated whether there exist degradation pathways other than the above-mentioned ones. By concurrently inhibiting both sides of proteasomes using CD5083 and Tomatine, we observed NSGs enlargement compared to control (Fig. 8H), which ruled out the presence of compensatory degradation pathways. Inhibition of 20S proteasome activity alone had a negligible influence on NSG stability, confirming the dormant state of this degradation pathway under the modulation of functionally intact VCP (Fig. 8J). Additionally, we explored whether similar dissociation actions can be extended to c-SGs. According to literature, SGs induced by heat stress typically undergo VCP-mediated degradation for resolution[36]. We thus assessed the effect of 19S proteasome on the condensation of G3BP1 in heat-stressed cells. A rescue effect exerted by CB5083 on SGs was observed, excluding the presence of alternative degradation pathways in this context (Fig. 8I), which supports the specificity of dual-degradation pathways only in cases associated with nanomaterials.

Potential of NSGs in remodeling chemo-plasticity

We further examined the potential biological functions of NSGs. By introducing a VCP inhibitor, we found an effective way for NSGs-

https://doi.org/10.1038/s41467-025-64623-4

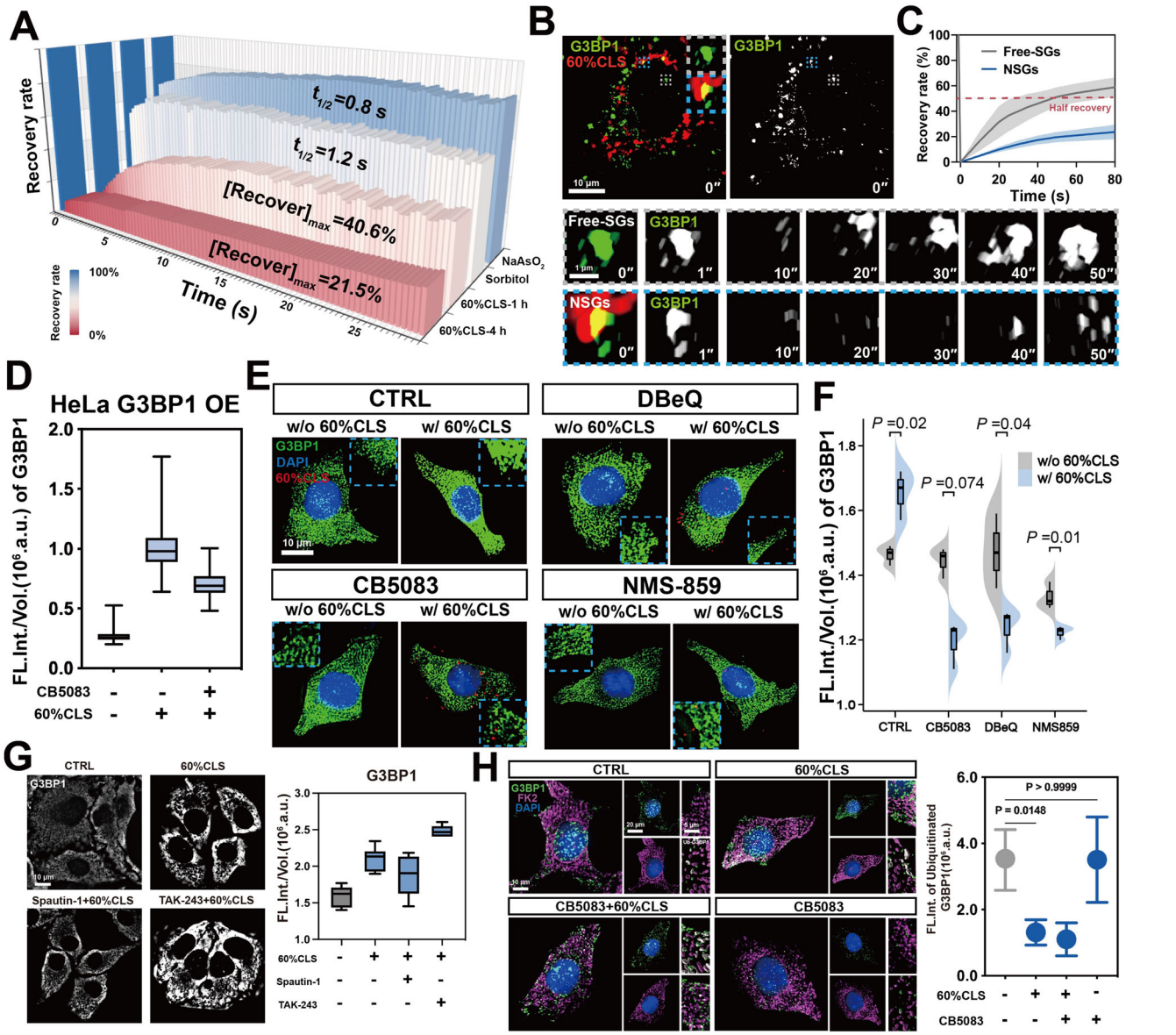

Fig. 7 | NSGs disassembly. A Recovery rate of SGs as a function of time in cells receiving different stimulations, as measured by using FRAP. **B** Representative fluorescence graphs and **C** recovery curves of free SGs (marked by a gray dashed box) and NSGs (blue dashed box). **D** Condensation of NSGs in cells overexpressing *G3BP1*. Fluorescence of NSGs in cells receiving nanomaterials with or without CB5083 treatment was calculated and normalized by the volume of each droplet, as plotted. **E** Immunofluorescence graphs and **F** condensation information of NSGs in cells received different treatments. A set of VCP-p97 inhibitors, including DBeQ, CB5083, and NMS-859, was considered. Control (CTRL) stands for VCP-intact cells. Inset: Enlarged view of randomly depicted region as highlighted by the dashed blue square. **G** Association of ubiquitination with NSGs integrity. Deubiquitinase inhibitor (Spautin-1) and ubiquitin activating enzyme (E1) inhibitor (TAK-243) were leveraged in combination with nanomaterials. **H** Ubiquitination levels of G3BP1. In this case, ubiquitinated proteins were labeled by an antibody (clone: FK2) that was pseudo-colored in magenta, alongside nucleus counterstaining with DAPI (blue). Statistical differences were calculated using a two-tailed *t*-test or one-way ANOVA. Data represents mean ± SD (**D**, >300 G3BP1 puncta per group from 3 independent biological replicates; **A**, **C**, **F**, and **H**, $n = 3$ independent biological replicates). Source data are provided as a Source Data file. (**D**, **F**, **G**, and **H**, arbitrary units: a.u.).

specific dissociation to assess their biological implications by using RNA-sequencing. Subsequently, bioinformatic analysis, as shown in Fig. 9A, suggests that NSG inhibition compensatively activates multiple pathways, including MAPK and PI3K-Akt, which feature the highest enrichment factors (Fig. 9B). Given their pro-survival characteristics, it is hypothesized that NSG generation plays a role in maintaining cellular homeostasis under stress conditions induced by nanomaterials. To evaluate this hypothesis, assays were performed in which cells exposed to nanomaterials designed to induce NSGs were treated with pro-apoptotic or pro-inflammatory agents. As shown in Supplementary Fig. 17A, the presence of NSGs was associated with reduced activation of inflammatory and apoptosis pathways, indicated by lower nuclear translocation of NF-κB and reduced expression of cleaved caspase 8. When NSGs were depleted using CB5083, the observed effect of nanomaterials was not present, indicating that the pro-survival outcome was attributable to the presence of NSGs. Additionally, changes in mRNAs associated with microtubules were noted due to NSG dissipation. During SGs' growth, clients are translocated to premature droplets via the microtubule network[3,38]. Interplay between NSGs and the cytoskeleton suggests that, despite differences in composition and fluidity, both types of SGs exhibit similarities during their growth stages.

https://doi.org/10.1038/s41467-025-64623-4

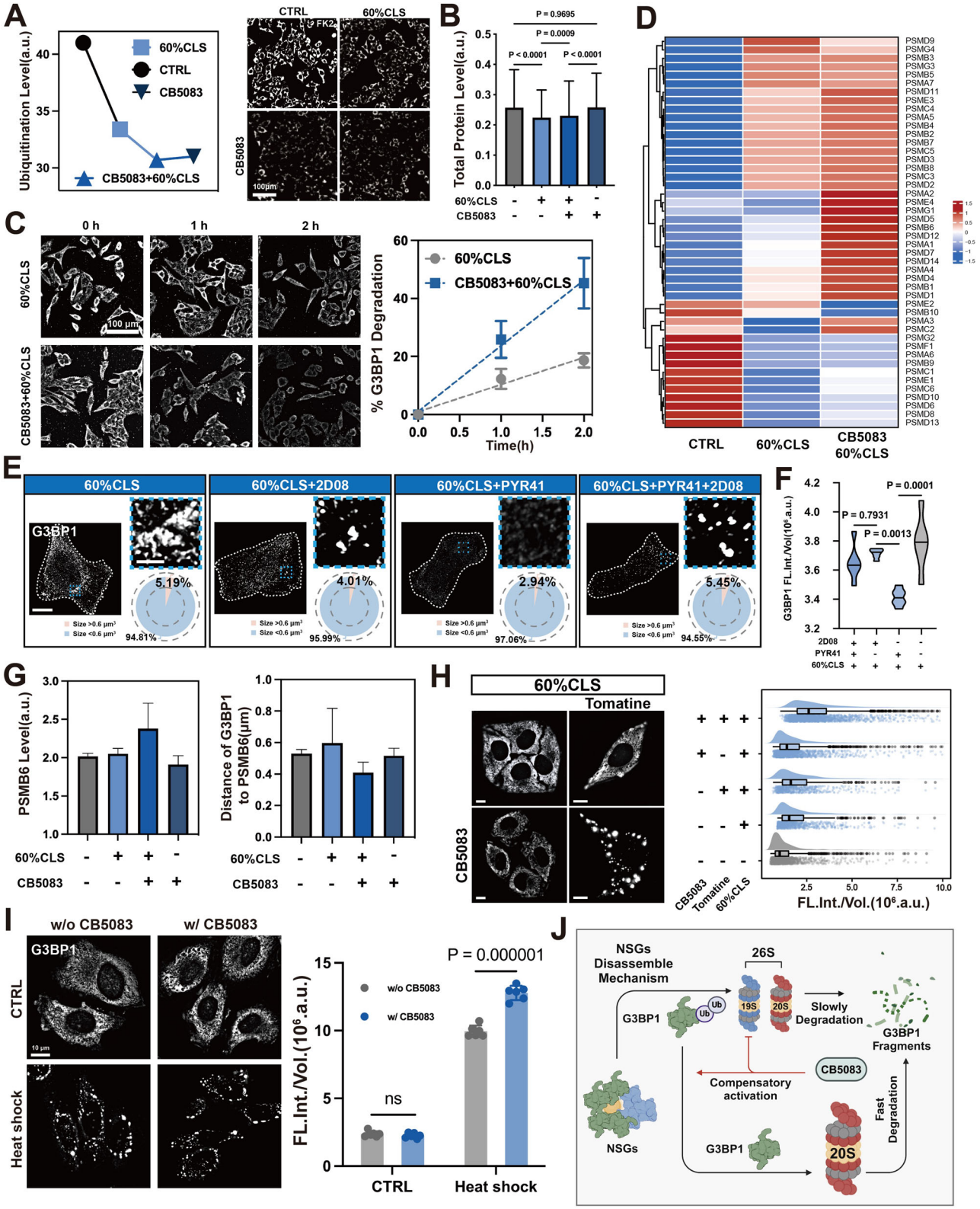

Recent research highlighted that by sequestering biomolecules (such as untranslated mRNA or proteins) and thus affecting their abundance and function, SGs can act as central hubs governing the chemo-plasticity of cells[39]. This raises the question of whether NSGs have similar implications and if this feature could be used for chemo-plasticity intervention. Therefore, we evaluated the cytotoxic effects of four chemotherapeutics alongside NSGs. Starting with Doxorubicin, a widely used drug that functions as a replication inhibitor, we analyzed Cleaved PARP expression levels as indicators of DNA damage. Upon introducing the VCP inhibitor, NSGs underwent rapid degradation mediated by the 20S proteasome, and a significant increase in Cleaved PARP levels was observed (Fig. 9C, 2.06-fold of control). These findings indicate that NSGs considerably mitigate the cytotoxicity caused by Doxorubicin in cancer cells.

We examined the impact of NSGs on chemo-plasticity in response to microtubule-targeting agents. Nocodazole and Paclitaxel, which

Fig. 8 | SUMOylation-dependent 20S pathway underlies NSGs dissociation. **A** Analysis of global ubiquitination levels of proteins. Ubiquitinated components were immunofluorescently labeled as shown on the right. **B** Total protein-level labeled with SRB in cells as described in (A) (Data points were hidden from presentation to ease the visualization of median value, entire information can be found in source data, $n > 4000$ G3BP1 puncta per group from 3 independent biological replicates). **C** Analysis of G3BP1degradation rates. Cells received 60% CLS-AuNPs in the presence or absence of CB5083 were assessed at 0 h, 1 h, and 2 h post-treatment. **D** A heatmap displays variation in the expression level of PSM family members. **E** Immunofluorescence graphs depict the impact of SUMOylation on the formation of NSGs in cells receiving 60%CLS-AuNPs and **F** quantitative results. In the pie chart (lower panel), the pink section represents the percentage of NSGs featuring a volume greater than 0.6 μm^3. Scale bars: 10 μm and 2 μm for the entire cell and the magnified zone, respectively. **G** Expression of PSMB6 (left panel) and its interaction with G3BP1 as reflected by their distance (right panel, data points were hidden from presentation to ease the visualization of median value; the entire information can be found in the source data). **H** Analysis of the NSGs-promotion effect of 60% CLS-AuNPs in 19S- and/or 20S-activity suppressed cells ($n > 500$ G3BP1 puncta per group from 3 independent biological replicates). Quantitative results of G3BP1 condensation extent are presented on the right side. Scale bars: 10 μm. **I** Immunofluorescence graphs and quantitative results of G3BP1 condensation in heat-stressed cells in the presence or absence of CB5083. **J** A schematic illustrating the dual-mode disassembly mechanism of NSGs. Created in BioRender. Huo (2025) https://BioRender.com/9a10tni. Statistical differences were calculated using a two-tailed *t*-test or one-way ANOVA. Data represents mean ± SD (Independent biological replicates for **A**, **C**, **F**, **G**, and **I**, 3, 7, 6, 3, and 6, respectively). Source data are provided as a Source Data file. (**F**, **G**, and **I**, arbitrary units: a.u.).

function differently, were introduced as presented in Fig. 9D. It was observed that nanomaterials alone intensified the microtubule depolymerization caused by nocodazole at concentrations of 50 nM or higher. Introduction of VCP inhibitor mitigated this effect on the cytoskeleton, as indicated by morphology (Fig. 9E, sphericity values: 0.65, 0.78, and 0.95 for 60% CLS, 1 nM, 50 nM, and 100 nM; Supplementary Fig. 17B, isotropy values: 0.61, 0.51, and 0.37 for 60% CLS, 1 nM, 50 nM, and 100 nM, respectively), highlighting the role of NSGs as nocodazole-sensitizers in chemo-plasticity remodeling. Conversely, when paclitaxel, a stabilizer of polymerized microtubules, was used instead of nocodazole, the presence of NSGs reduced the effectiveness of the chemotherapeutic (Fig. 9E, F). These findings suggest that NSGs can modify the chemo-plasticity of cancer cells, making them more sensitive to microtubule depolymerization. This analysis was replicated in cisplatin-treated cells (Fig. 9G), showing reduced expression of the DNA damage biomarker γ-H2AX (Fig. 9H, expression levels: 0.97, 0.73, and 0.87 for nanomaterials combined with cisplatin at 10 μM, 50 μM, and 250 μM, respectively), which returned to basal level upon NSG dissociation. These results indicate that NSGs' effects on cancer chemo-plasticity are context-dependent (Fig. 9I). For nocodazole, NSGs may enhance its sensitizing effect for tumor management. For other chemotherapeutics, combination with CLS-AuNPs could potentially reduce unwanted cytotoxicity, especially in healthy tissues like the liver. To test this hypothesis further, our subsequent studies will explore the pro- and anti-chemo-action effects of nanomaterials in cancerous and normal tissues, respectively.

In vivo implications of NSGs

Previous experience showed a correlation between the organ distribution of injected nanomaterials and their hydrophilicity. To identify the tissues for chemo-toxicity mitigation, we assessed nanomaterial enrichment over time post administration. We focused on the liver, spleen, and kidney due to their higher likelihood of enriching nanomaterials. Accumulation of AuNPs in tissues was confirmed shortly after administration, which increased consistently over time. The liver had the highest enrichment (maximal accumulation: 40.9% at 48 h), followed by the spleen (16.7% at 48 h) and kidney (7.2% at 24 h). The presence of nanomaterials is essential for NSGs provocation. However, it is unclear whether nanomaterials enriched in certain tissues preserve such potential and their contribution to chemo-toxicity mitigation. We evaluated tissue responses to Doxorubicin, cisplatin, and paclitaxel. Nanomaterials reduced drug side effects as indicated by the lower levels of damage-related biomarkers. Thus, nanomaterial presence ensured NSG generation with biological implications in vitro.

We proceeded to assess the feasibility of using NSGs-regulated chemo-plasticity for solid tumor management. A xenograft animal model was established as illustrated, and CLS-AuNPs were intratumorally administered once the volume of tumor tissue reached a certain value (Fig. 10C, Trial#1, Supplementary Fig. 18A, B). Subsequently, systematic administration of nocodazole at differing dosages (denoted by 0.5× and 1×) was conducted (I–V as illustrated). Both the growth curves of the solid tumors and the overall survival of mice receiving corresponding treatments were recorded. Results indicated that the presence of NSGs, even when the dosage of chemotherapeutics was halved (group I), exerted enduring yet robust tumoricidal effects, outperforming the outcome of chemotherapy alone at normal dosage (group III). Abrogation of anti-tumoral action was observed when nanomaterials were employed alone for disease management, further supporting that the observed tumor regression should be attributed to the synergistic action between chemo-plasticity remodeling and nocodazole. To assert this conclusion, cell lines devoid of G3BP1 were employed for xenograft establishment. After replicating the above treatment, tumor tissues were collected and dissociated into single-cell suspensions for flow-cytometry analysis (labeling with Annexin V-FITC/PI for gating). In wild-type tissues, the viability of solid tumors receiving varying treatments (I, III, and V as representatives, viability: 45.1%, 69.2%, and 94.7%, respectively) corresponded with their growth rates. Notably, the knockout of G3BP1 substantially weakened the anti-tumoral effect of treatment I ($HeLa^{G3BP1\ KO}$), confirming that NSGs, rather than nanomaterials, underlie the sensitized chemotherapy.

Furthermore, the capacity of nanomaterials to protect liver tissue from systemic chemotherapy-associated side effects in tumor-bearing animals was analyzed (Fig. 10D, Trial#2). Cisplatin was selected for the study due to its notable liver toxicity, and necropsy and immunofluorescence imaging were conducted to decipher the tissue damage at the bulk and cellular levels, respectively. Typically, cisplatin-induced liver damage caused the accumulation of apoptotic hepatocytes in lobules, characterized by fragmented nuclei surrounded by vacuoles (inset necropsy, IV group). The proportion of damaged tissues due to cisplatin exposure was quantified, and results demonstrated that the co-presence of nanomaterials markedly mitigated the liver toxicity of the drug (%damaged region: 42% and 10% for chemotherapy alone and with nanomaterials, respectively). Expression levels of DNA damage markers (Cleaved PARP) further confirmed the liver-protective function of nanomaterials. As there existed the possibility that mitigation of liver toxicity with nanomaterials proceeds in an NSG dispensable manner, liver-specific adeno-associated virus serotype 8 (AAV8) carrying TBG (thyroxine-binding globulin) promoter and shRNA targeting G3BP1 and hnRNPC (Fig. 10E, AAV denoted by #1 and #2, respectively), two components integral to the establishment of NSGs, were employed. Recorded serum biomarkers indicated that knockdown of each protein in the liver reduced the protective effect exerted by nanomaterials to a comparable extent, safely attributing the mitigated chemo-toxicity to NSGs.

During the systematic exposure to nanomaterials and chemotherapeutics, serum was collected for immune response assessment. Using an antibody array, the expression levels of pro-inflammatory cytokines in peripheral circulation were analyzed. Dye-labeled blots can be found in Fig. 10F and Supplementary Fig. 18C, with

https://doi.org/10.1038/s41467-025-64623-4

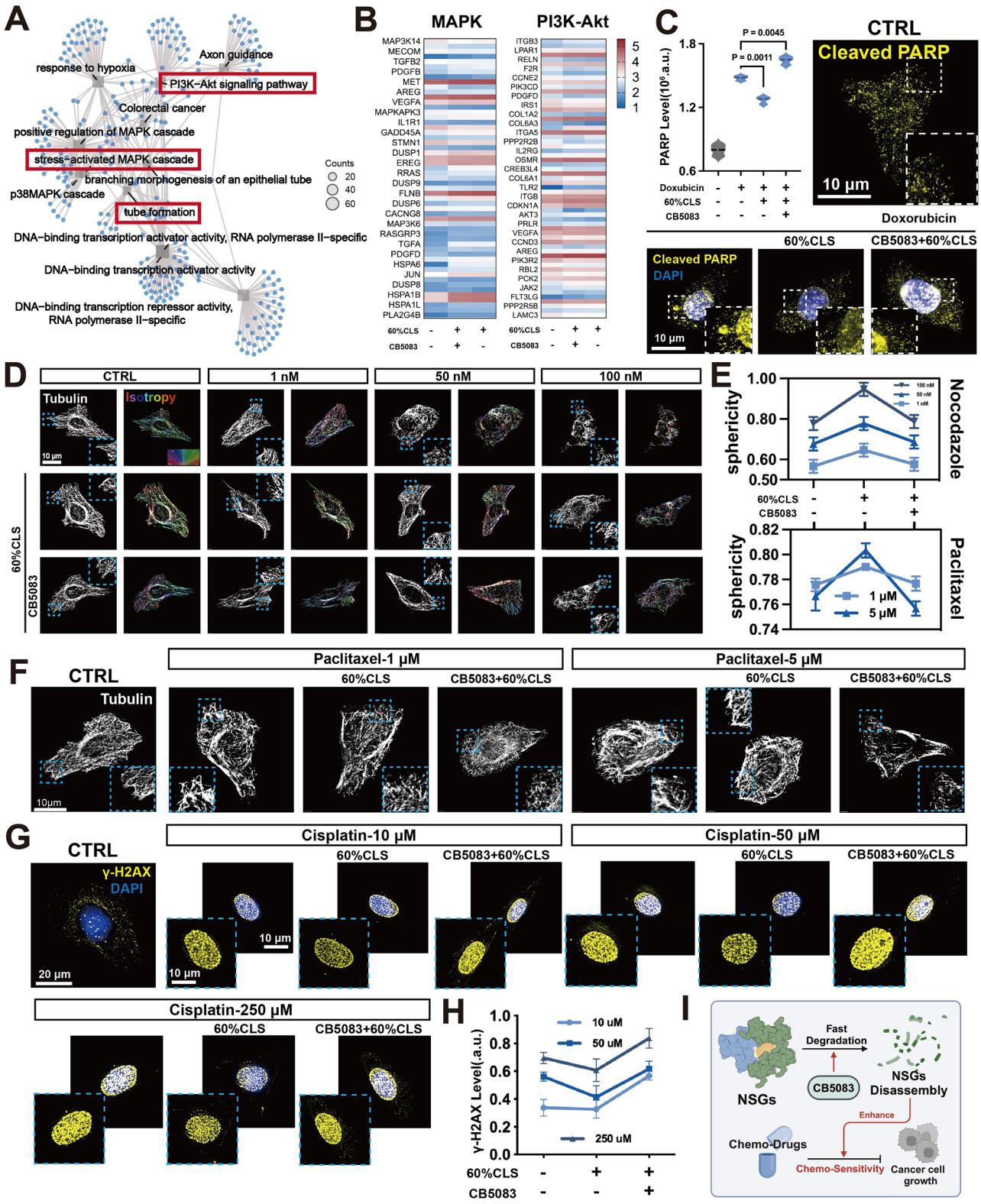

results ruling out the prevalence of an inflammatory response (Fig. 10G). Additionally, it was confirmed that exposure to nanomaterials caused negligible changes in organs beyond the liver, as indicated by intact tissue morphology (Supplementary Fig. 19). These findings collectively ensured the safe usage of CLS-modified nanomaterials for local chemo-plasticity reshaping and thereby modulating the therapeutic outcome.

Discussion

Nanomedicines have been extensively utilized for disease management. Most research efforts focus on understanding the implications of certain nanotherapeutics at transcriptional and translational levels[40,41]. Upon exposure to nanomaterials, their outer surfaces are rapidly passivated by biomolecules both intra- and extracellularly, a phenomenon known as the protein corona effect (PCE)[42]. While PCE is

Fig. 9 | NSGs-modulated chemo-plasticity. A A network diagram revealing the biological implications of NSGs. In the network, the blue nodes (circular representations) denote genes, while the gray nodes (square representations) signify classes. The connecting lines illustrate the relationships between the various entries and genes, with the size of the entry nodes matching the number of gene counts in the corresponding term. **B** A heatmap illustrating DEGs associated with MAPK and PI3K-Akt pathways during the formation of NSGs (60% CLS-AuNPs, denoted by 60% CLS) and the activation of the compensatory degradation mode of NSGs (combinational treatment denoted by 60%CLS + CB5083). **C** Analysis of the expression levels of cleaved PARP (pseudo-colored in yellow) and corresponding fluorescence graphs of cells receiving chemotherapy alone or in combination with or without NSGs as stimulated by nanomaterials (arbitrary units: a.u.). **D** and **F** Morphological analysis of microtubules. Cells expressing intact NSGs (60% CLS alone) or their dissociated form (with CB5083) were treated with **D** nocodazole and **F** paclitaxel at different concentrations. The color bar stands for the direction the microtubules align. Inset: Enlarged view of randomly depicted region as highlighted by the dashed blue square. The sphericity of microtubules was measured as displayed in (**E**). **G** Representative fluorescence graphs and **H** quantitative results of the γ-H2AX. For the treatments, please refer to (**C**) for reference. Inset: Enlarged view of a randomly depicted region as highlighted by a blue dashed square (arbitrary units: a.u.). **I** A schematic illustration of the influence of NSGs on chemo-plasticity. Created in BioRender. Huo (2025) https://BioRender.com/op4mwz0. Statistical differences were calculated using a two-tailed *t*-test or one-way ANOVA. Data represents mean ± SD (Independent biological replicates for **C**, **E**, and **H**, 3, 6, and 3, respectively). Source data are provided as a Source Data file.

widely accepted as resulting from random protein condensation enclosing nanomaterials, recent findings suggest that PCE may be a highly regulated and preferential process[43]. Flexible proteins with intrinsic disordered regions are more likely to be adsorbed by nanomaterials compared to rigid ones. Once adsorbed, these flexible proteins undergo forcible unfolding to various extents depending on interactions with ligands functionalizing the nanomaterials, which cause their rigidity to reduce[44]. Such a process facilitates multivalency binding with bystander biomolecules, thus creating an environment that benefits the formation of MLOs. Despite these observations, the influence of specific types of MLOs on the action and metabolism of nanomedicine remains unclear. Herein, we provide compelling evidence demonstrating that suitably functionalized nanomaterials can induce the formation of NSGs, which differ compositionally and physicochemically from their canonical counterparts.

For different types of SG subtypes (e.g., heat-shock-induced or AS-induced), although they differ in composition, a mild-to-moderate stress condition is required for their generation. Despite the difference in stimulation, c-SGs generally initiate from the nucleation of RNP-mRNA complex, followed by its growth through recruiting client proteins that establish a liquid-like coacervated droplet[3]. Less is known about non-canonical SGs that originate under stress-free conditions. Through stepwise all-atom simulations, it was shown that the sequential recruitment of hnRNPC and G3BP1, mediated respectively by multivalency interactions between CLS-hnRNPC and $Coil_{111\text{-}123}$ residue (hnRNPC) and NTF2L domain (G3BP1), can promote NSGs formation in the absence of stress. Truncation and KO assays confirmed that the sequential phase separation of hnRNPC and G3BP1 is crucial for NSGs formation. While secondary phase separation within already established MLO is observed in FUS, Tau, and TDP43-composed counterparts[45,46], there is no similar observation during the growth stage of SGs, whose client components were previously believed to be recruited in parallel[5]. Intriguingly, both NSGs and dysfunctional MLOs observed in functionally degenerative neurons feature less fluidity with respect to conventional counterparts like SGs, revealing that the sequential phase separation might be crucial for establishing a more closely packed microstructure. Our findings collectively suggest a seeded-growth-like mechanism underlying the growth of NSGs, termed tri-phase separation. Future research is encouraged to investigate the possibility of sequential phase separation occurring during the nucleation stage of other MLOs beyond SGs.

With the advancement of imaging modality, the microstructure of MLOs can be revealed in more detail regarding composition information. For the function executed by MLOs, predictions are made based on a collective consideration of physical, chemical, and biological features, although proper methods to assess the former two are still lacking[1]. To address this challenge, a biorthogonal functional imaging approach was developed in this study using HaloTag-rendered, NSGs-specific imaging. By introducing physicochemical microenvironment-responsive, Halo-ligand-conjugated dyes, a set of parameters, including local temperature, polarity (physical parameters), pH, and proteasome activity (chemical parameters), was analyzed. Despite physical similarities between NSGs and canonical counterparts, their sub-SGs distribution of G3BP1 differed significantly based on measured local pH. Additionally, it was found that proteasome enrichment levels in NSGs are higher than those in canonical counterparts. During SG disassembly, proteasome recruitment is typically associated with imminent dissociation via degradation of ubiquitinated scaffold proteins[36]. Therefore, the preservation of proteasome-collecting NSGs was unexpected. FRAP assays indicated that the gel-like structure of NSGs helps to hinder the interaction with proteasomes, thereby mitigating disassembly.

The disassembly of SGs can occur through ubiquitination or chaperone mediation. For ubiquitination, G3BP1 interacts with VCP-p97, leading to its proteasomal cleavage[36]. In the chaperone-mediated pathway, HSP70 and HSP90 force refolding of scaffold proteins, destabilizing droplets[47]. Inhibitor assays showed that chaperone pathways do not contribute to NSGs disassembly. Blocking the VCP function accelerates NSGs dissociation. Transcriptome and inhibitor assays confirmed dual modes of NSGs disassembly: VCP-mediated 19S proteasome acts slowly under normal conditions due to the gel-like structure of NSGs. Dysfunction of 19S leads to 20S proteasome compensating via SUMOylated G3BP1 recognition, speeding up NSGs disassembly. This finding aids in understanding non-canonical MLO disassembly and provides a precision inhibitor for modulating NSGs activity.

By manipulating NSGs using VCP inhibitors, their association with chemo-plasticity was confirmed. Subsequently, NSGs were leveraged as the chemosensitivity remodeling hub for in vivo applications. Striking a balance between the cytolytic effect on solid tumors and minimizing side effects on normal tissues has long been a challenging goal in clinical trials, often resulting in compromises in therapeutic outcomes. This study demonstrates that the site-specific provocation of NSGs holds promise for smart disease management. Specifically, for drugs whose efficacy is mitigated by NSGs, nanomaterial delivery stimulates these MLOs in liver tissues normally susceptible to therapeutic damage, thereby mitigating chemo-toxicity. Conversely, for drugs that synergize with NSGs, localized tumor introduction of nanomaterials provides a feasible yet robust method to reduce therapeutic dosage, achieving safe disease control in a biocompatible manner.

Research interests in targeting MLOs are increasing, particularly in the context of neurodegeneration due to the increasingly clarified association between disease progression and dysfunctional protein coacervates. Among various disease-related MLOs, hnRNPC and G3BP1 have been frequently highlighted, either through indirect association with disease progression as MLO scaffolds or direct contribution. As central compartments of NSGs, the potential of their generation in neurons to mitigate the liquid-to-gel transition of certain MLOs and optimize this process for disease management warrants further investigation. Another promising direction involves validating NSGs' ability to destabilize already solidified components. Existing evidence supports the possible translocation of components from

https://doi.org/10.1038/s41467-025-64623-4

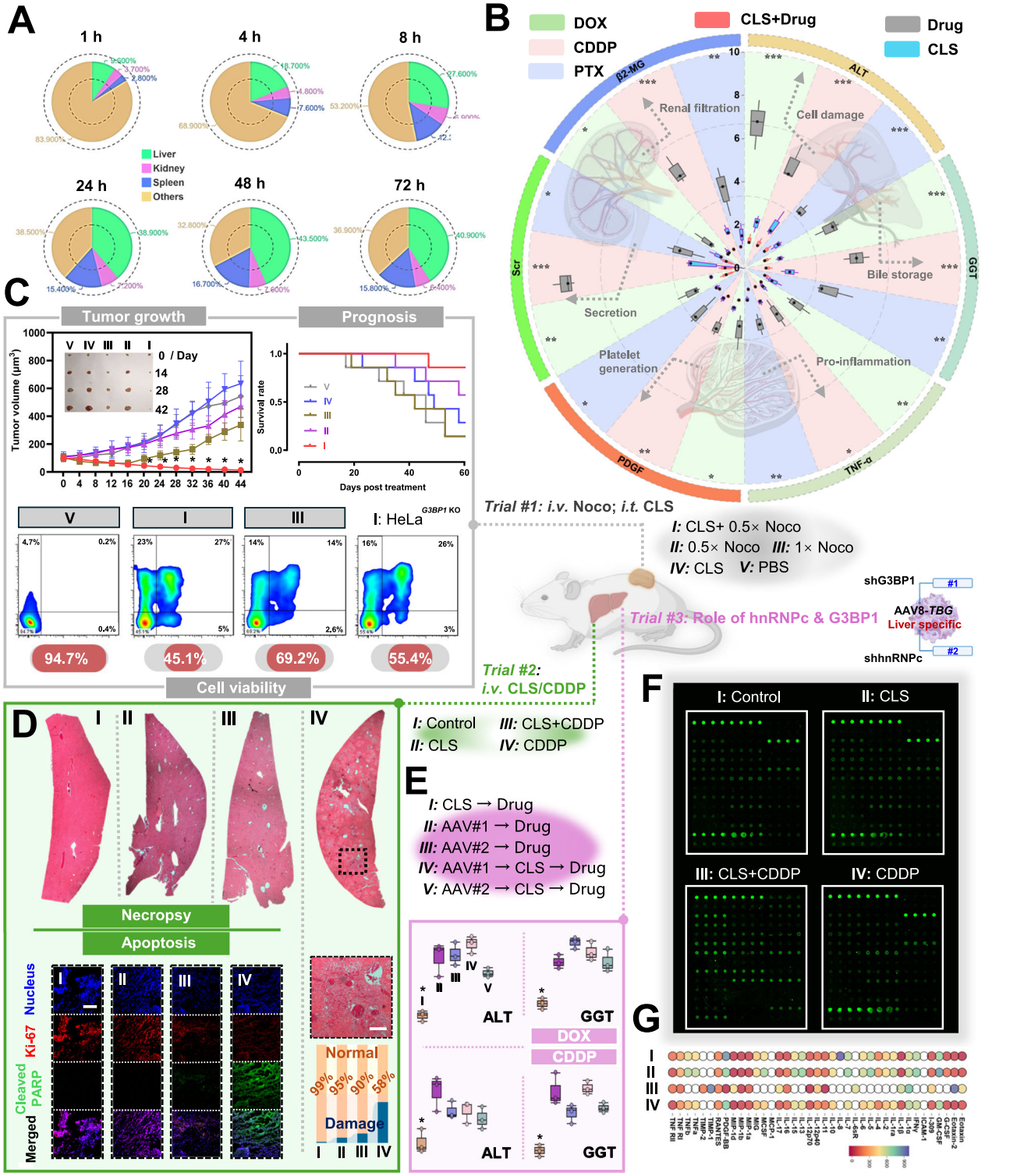

neurodegeneration-related granules to nanomaterials; however, precise control over this process remains unfulfilled. Sequential recruitment of candidate proteins via tailored functionalization of nanomaterials (as discussed herein and future designs beyond) may provide a pathway to targeted abrogation of MLOs through protein relocation. For nanomaterials within the size range examined in this study (30 nm and above), specific surface functionalization is required to enable blood-brain barrier permeability, which may reduce interactions between endocytosed nanomaterials and MLOs. One approach to address this involves utilizing established inter-organ communication pathways for drug delivery[48].

Nanotoxicity studies have extensively examined the biological effects of nanomaterials on transcription, translation, and metabolism. With more metastable cellular structures as MLOs, identified, understanding their interaction with nanomaterials in terms of nanotoxicity is just beginning. This study proposes a framework for identifying nanomaterial-associated MLOs and decoding their biological functions. Future research should investigate how certain nanomedicines

Fig. 10 | In vivo therapeutic outcome. A Pie charts show the distribution of administered nanomaterials in different tissues as a function of time. **B** Potential tissue toxicity caused by chemotherapeutic exposure. Damage in certain tissues was reflected by the measured level of biomarkers in serum. Created in BioRender. Huo (2025) https://BioRender.com/dqtszuh. **C** Trial#1: Overall anti-tumoral action of different treatments. For treatment with nocodazole (Noco) alone, 0.5× and 1× stand for the relative concentration of therapeutics. Flow-cytometry results revealing the cell viability can be found in the lower panel (cell viability). Single-cell suspension of solid tumor was prepared as illustrated in Supplementary Fig. 18A and B, followed by their staining with Annexin V-FITC and PI for apoptotic level measurement. Created in BioRender. Huo (2025) https://BioRender.com/nks3eyf. **D** Trial#2: Liver protection effect exerted by NSGs. Left panel: Bright field graphs of liver tissue (necropsy, left panel) were employed for assessing the proportion of damaged regions (lower right) in the whole lobule (upper right: enlarged graphs of a representative zone as marked by a black dashed square). Right panel: Immunofluorescence graphs of liver tissues. Proliferating hepatocytes and damaged cells were stained with Ki-67 (pseudo-colored in red) and cleaved PARP (green), alongside counterstaining with DAPI to visualize the nucleus. Scale bar: 200 μm. **E** Trial#3: Mechanism exploration. Tumor-bearing mice were subjected to liver-conditioned knockdown of hnRNPC or G3BP1, and the damage caused by chemotherapeutics, including doxorubicin (DOX) and cisplatin (CDDP), was measured as reflected by the expression level of ALT and GGT. **F**, **G** Pro-inflammatory response induced by nanomaterials. Expression levels of representative cytokines in the peripheral circulation system of mice that received nanomaterials were measured using fluorescence antibody arrays. Unprocessed, dye-labeled blots (**F**) and the quantitative results (**G**) were provided. For the spatial distribution information for each cytokine on the blot, please refer to Supplementary Fig. 18C. Data represents mean ± SD (Independent biological replicates for **B**, **C**, **E**, and **G**, 3, 7, 3, and 4, respectively). Statistical differences were calculated using a two-tailed *t*-test. * indicates $P < 0.05$. Source data are provided as a Source Data file.

affect the homeostasis of MLO networks in organs beyond tumor tissues, such as the liver, which accumulates most intravenously injected nanomaterials. These findings could provide insights into therapeutic potentials akin to NSGs or inform the design of safer next-generation nanomedicines. Additionally, although cytotoxicity linked to ultrafine nanomaterials has been reported[14], this phenomenon is often attributed to oxidative stress. The extent to which ultrasmall nano-vehicle-induced MLO reprogramming contributes to cytotoxicity remains unclear and requires further investigation.

Our study also presents several limitations. While our all-atom MD simulations provide mechanistic insights into NSG formation, we must acknowledge the inherent limitations of computational modeling at nanomaterial-biointerfaces as an emerging frontier. Current force fields face challenges in accurately parameterizing dynamic ligand–protein interactions, necessitating ongoing methodological refinement. Future studies could enhance physical accuracy by integrating machine learning potentials[49]. Due to reproducibility and biosafety concerns, we utilized noble metal-based nanomedicine, whose cost-effectiveness should be carefully evaluated before clinical translation. Additionally, the impact of NSGs on other therapeutics, particularly recently emerged precision drugs targeting the immune system, should be explored in future studies to expand the applicability of our therapeutic approach. Furthermore, while we focused on the protective effects of nanomaterials on the liver, spleen, and kidneys, evaluating therapeutic benefits in other tissues and disease models beyond cancer that involved an expanded cohort will help establish a more comprehensive understanding of NSG-induced chemo-plasticity reprogramming.

In conclusion, our study provides valuable insights into the MLO-nanomaterial interplay network, systematically evaluating the formation/dissociation mechanisms of NSGs and their microstructure details at multiple levels. Our findings enhance the understanding of nanomedicine, providing guidelines for future design of precision therapeutics. We also hope the study can inspire further exploration of promising methodologies to harness the therapeutic potential of artificial MLOs.

Methods

Ethical statement

This study was approved by the Experimental Animal Care and Use Committee of Affiliated Nanjing Drum Tower Hospital of Nanjing University Medical School (2023AE01016).

Chemicals and antibodies

Gold (III) chloride trihydrate ($HAuCl_4{\cdot}3H_2O$, ≥99.9%), ascorbic acid (AA, ≥99.0%), sodium borohydride ($NaBH_4$, ≥98%), sodium bicarbonate ($NaHCO_3$, ≥99.5%) hexadecyltrimethylammonium bromide (CTAB, ≥99%), hexadecyltrimethylammonium chloride (CTAC, 25% wt/vol), sodium arsenite ($NaAsO_2$, ≥90%) Bovine serum albumin (BSA) and lipopolysaccharides (LPS, Escherichia coli O55:B5) were all obtained from Sigma–Aldrich (United States). D-Sorbitol solution, dimethyl sulfoxide (DMSO, anhydrous), Cy5-PEG_{2k}-SH, NHS-PEG_{5k}-SH, FA-PEG_{1k}-SH, 4-[3-(Trifluoromethyl)-3H-diazirin-3-yl] benzylamine hydrochloride (≥98%), potassium iodide (KI, ≥99%), iodine (I_2, ≥99.8%), puromycin dihydrochloride (≥98%), doxorubicin hydrochloride (98%), nocodazole (≥98%) and Streptavidin were all obtained from Aladdin (P.R. China). Paclitaxel (98%), cisplatin (65%), coumarin (98%), Iron (II) chloride tetrahydrate ($FeCl_2{\cdot}4H_2O$, ≥98%), Iron (III) chloride ($FeCl_3$, ≥99%), Ammonium hydroxide solution (28 wt% NH_4OH), (3-Aminopropyl)triethoxysilane (APTES, ≥99%) were purchased from Macklin (P.R. China). OMe-PEG_{1k}-SH, OMe-PEG_{5k}-SH, OMe-PEG_{10k}-SH, OMe-PEG_{20k}-SH, OMe-PEG_{30k}-SH, OMe-PEG_{40k}-SH, COOH-PEG_{5k}-SH, and NH_2-PEG_{5k}-SH were purchased from JenKem Technology (P.R. China). CLS-PEG_{5k}-SH was purchased from YusiYY (P.R. China). Protonex Red 600 was purchased from KeyGEN BioTECH (P.R. China). Rhodamine B (97%), Tetrazine-sulfo-NHS ester, and TCO-Biotin were purchased from Bidepharm (P.R. China). HaloTag ligand (2-(2-(6-chlorohexyloxy) ethoxy) ethanamine hydrochloride, 97%) and LLVY-AMC-N_3 were purchased from Picass (P.R. China). TAK-243, Spautin-1, Myricetin, Grp94, AMP-PCP, CB5083, DBeQ, 2-D08, NMS-859, PYR-41, tomatine, and etoposide were all purchased from MedChemExpress (MCE, United States). All chemicals and solvents are used as received without further purification. Nuclear stain DAPI, Dulbecco's Modified Eagle Medium (DMEM), phosphate-buffered saline (PBS), penicillin/streptomycin (100×), and fetal bovine serum (FBS) were obtained from Invitrogen (Thermo Fisher Scientific, United States). Deionized (DI) water with a resistivity of 18.2 MΩ·cm was used in all experiments, which was prepared using an ultrapure water system (Arium Mini, Sartorius, Germany). Primary antibodies: Anti-BiP Rabbit mAb (#3177, 1:400, Cell Signaling, United States), anti-CHOP Mouse mAb (#2895, 1:400, Cell Signaling), anti-G3BP1 Rabbit mAb (#61559, 1:400, Cell Signaling), Alexa Fluor 488-conjugated anti-G3BP1 Rabbit mAb (#94496, 1:400, Cell Signaling), anti-G3BP1 Mouse mAb (66486-1-LG, 1:500, Proteintech, P.R. China), anti-hnRNP C1/C2 Rabbit mAb (ab133607, 1:500, Abcam, UK), anti-ubiquitinated protein Mouse mAb (04-263, 1:200, Merck, Germany), anti-Cleaved PARP (Asp214) Rabbit mAb (#5625, 1:500, Cell Signaling), anti-Caspase8 Mouse mAb (#9746, 1:500, Cell Signaling), Alexa Fluor 647-conjugated anti-gamma H2A.X (ab195189, 1: 200, Abcam), Alexa Fluor 488-conjugated anti-Alpha Tubulin Mouse mAb (322588, 1:500, Invitrogen), anti-PSMB6 Rabbit mAb (GTX23331, 1:200, Genetex, United States), anti-Albumin Rabbit mAb (ab207327, 1:2000, Abcam), anti-NF-κB p65 Rabbit mAb (#8242,1:800, Cell Signaling), anti-Cleaved Caspase3 Rabbit mAb (#9664, 1:1000, Cell Signaling). Secondary antibodies: Alexa Fluor-488-labeled goat-anti-rabbit IgG (H+L) cross-adsorbed secondary antibody (A-11008, 1: 500, Invitrogen), Alexa Fluor 555-conjugated goat-anti-rabbit IgG H&L (#4413, 1:1000, Cell Signaling), Alexa Fluor 488-conjugated goat-anti-mouse IgG H&L (#4408, 1:1000, Cell

Signaling), anti-Rabbit IgG, HRP-linked Antibody (#7074, 1:3000, Cell Signaling).

Synthesis and functionalization of Au nanospheres

AuNPs were synthesized using the seed-mediated growth method[17]. Briefly, gold nanoseeds were prepared by mixing $HAuCl_4$ (0.5 mM), $NaBH_4$ (10 mM), and CTAB (200 mM), followed by vortexing for 2 min until the solution turned brown. The mixture was incubated at 37 °C for 3 h to decompose excess $NaBH_4$. For 10 nm AuNPs, gold nanoseeds were added to a growth solution containing $HAuCl_4$ (0.5 mM), CTAC (200 mM), and ascorbic acid (100 mM), followed by 30 min incubation with shaking. Larger AuNPs (30–180 nm) were obtained through iterative seed-mediated growth with controlled injection of $HAuCl_4$ (0.5 mM) at 2 mL/h using a syringe pump. Particle size and morphology were characterized by TEM (JEM-1400, JEOL, Japan) and UV-vis spectroscopy (1800PC, JingHua, P.R. China).

For charged AuNPs, NH2-PEG-SH and COOH-PEG-SH were added into the aqueous solution of freshly obtained nanospheres to reach a final concentration of 10 μg/mL. After 4 h vortexing, FA-PEG-SH and Cy5-PEG-SH were added and incubated overnight. The product was collected by centrifugation at 15,000 × *g* for 15 min, washed once with water, and re-dispersed in deionized water to OD ~ 5.

For CLS-PEG-SH modification, CLS-PEG-SH and OMe-PEG-SH were mixed at varying ratios (ranging from 20% to 100%) with AuNPs, followed by FA-PEG-SH/Cy5-PEG-SH addition. For photo-crosslinkable AuNPs, diazirine-conjugated-PEG-SH was synthesized by reacting 4-[3-(Trifluoromethyl)-3H-diazirin-3-yl] benzylamine hydrochloride with NHS-PEG-SH in $NaHCO_3$ (pH~8.0) at 4 °C overnight, then mixed with AuNPs and functionalized as above.

Cell culture and treatments

Human cervical carcinoma cell line (HeLa) was obtained from American Type Culture Collection (ATCC, P.R. China) and cultured in the growth medium of Dulbecco's Modified Eagle's Medium supplemented with 10% FBS and 1% penicillin/streptomycin. Cells were cultured at 37 °C under 5% CO_2 in a humidified incubator (MCO-170AICUV-PE, PHC, Japan). Upon reaching ~85% confluency, cells were trypsinized using 0.25% trypsin (KeyGen Biotech, P.R. China) and passaged for further experiments. For stress granule induction, cells were treated with: sodium arsenite (AS, 0.3 M, 30 min), sorbitol (0.4 M, 90 min), or various functionalized AuNPs (OD ~ 5, 1:100 dilution in complete media for 4 h unless otherwise specified). Inhibitors were applied at: myricetin (50 μM, 3 h), ML346 (20 μM, 4 h), Grp94 (4 nM, 4 h), AMP-PCP (50 μM, 4 h), spautin-1 (10 μM, 4 h), TAK-243 (1 μM, 20 min), CB5083 (10 μM, 30 min), DBeQ (10 μM, 4 h), NMS-859 (5 μM, 6 h), Tomatine (5 μM, 4 h), 2-D08 (200 μM, 24 h), PYR-41 (10 μM, 4 h), LPS (5 μg/mL, 24 h) and Etoposide (50 μM, 24 h). Chemotherapeutic agents were administered at: Nocodazole (1, 50, or 100 nM, 2 h), Paclitaxel (1 or 5 μM, 4 h), and Doxorubicin (2 μM, 2 h). For heat stress, HeLa cells in an 18-well plate (ibidi, Germany) were incubated at 42 °C with 5% CO_2 for 1 h.

Transfection

The SLenti-CMV-EGFP-G3BP1-puro lentivirus was purchased from OBiO (TS0517, P.R. China), for sgRNA plasmids (sgRNA sequence: CTCATTAACATACTGAACGA):

5′-ATGGACTATCATATGCTTACCGTAACTTGAAAGTATTTCGATTTCTTGGCTTTATATATCTTGTGGAAAGGACGAAACACCGCTCATTAACATACTGAACGAGTTTTAGAGCTAGAAATAGCAAGTTAAAATAAGGCTAGTCCGTTATCAACTTGAAAAAGTGGCACCGAGTCGGTGCTTTTTTG-3′

It was provided by Beyotime (L02615, P.R. China). Truncated G3BP1 plasmids were constructed by Tsingke Biotech (P.R. China). CO., Ltd (Contact Da Huo for reasonable sharing request). In a typical assay, HeLa cells were seeded at 1×10^5 cells per well. After overnight culture at 37 °C with 5% CO_2, cells reaching 30%–50% confluency were transfected with lentivirus at MOI = 10 in fresh medium containing polybrene (final concentration 5 μg/mL). Following 24-h incubation, the viral supernatant was replaced with complete medium. At 48 h post-transfection, EGFP-G3BP1 expression was preliminarily assessed by fluorescence microscopy. When cell density reached 50%–70% confluency, selection was initiated using 1 μM puromycin-containing medium for one week to establish stable transductions.

DL-Stbl3 competent cells (DLC106, Tsingke Biotech) were transformed with the *hnRNPC* KO plasmid following the standard heat-shock protocol. Positive clones were expanded in LB/ampicillin, and plasmids were purified using a commercial kit (I613KA4995, Sangon Biotech, P.R. China) following the manufacturer's instructions. For plasmid transfection, HeLa cells were seeded at 5×10^3 cells/well in chamber slides and allowed to reach 50%–70% confluency. Plasmid DNA (1 μg) was delivered using Lipofectamine LTX (A12621, Thermo Fisher Scientific) according to the manufacturer's instructions, with transgene expression assessed 24-48 h post-transfection.

AAV8-TBG-vehicle was a kind gift from Dr. Pengxiang Min; the corresponding sequence is as follows:

shG3BP1 sequence: (target: CGGGAATTTGTGAGACAGTAT)

5′- CCGGCGGGAATTTGTGAGACAGTATCTCGAGATACTGTCTCACAAATTCCCGTTTTT -3′

shhnRNPC sequence: (target: GCCTTCGTTCAGTATGTTAAT)

5′- CCGGGCCTTCGTTCAGTATGTTAATCTCGAGATTAACATACTGAACGAAGGCTTTTT -3′

Fluorescence imaging and data processing

Cells were fixed with 4% paraformaldehyde (P0098, Beyotime) for 10 min at room temperature and washed three times with PBS. Subsequently, cells were permeabilized with 0.1% Triton X-100 (*v/v*, 9036-19-5, Sigma) in PBS for 15 min before blocking with PBS containing 5% goat serum for 1 h at room temperature. Target proteins were immuno-stained with diluted primary antibodies overnight at 4 °C, followed by incubation with appropriate secondary antibodies (except when using directly labeled primary antibodies). Fluorescence imaging was performed using a TIRF microscope (Thunder Imager with Infinity TIRF system, Leica, Germany) equipped with 405 nm, 488 nm, 561 nm, and 638 nm lasers and a 100× plan-Apochromat objective (NA 1.47). Cells grown in 18-well glass-bottom dishes (ibidi) were imaged in epi mode. Acquired images were processed using Leica LAS X software (version 3.2.1) for computational clearing and deconvolution, achieving final resolutions of 136 nm (x-y axis) and 300 nm (z-axis). Three-dimensional reconstruction and quantitative analysis were performed using Imaris software (version 9.9, Oxford Instruments, UK) with Surface, Spot, and Cell modules, applying consistent thresholds. The analysis included measurements of: Total object volume, intensity mean, shortest distance to recognized surface, sphericity, and colocalization. Isotropy of microtubules was quantified using ImageJ software with FibrilTool and OrientationJ plugins.

Fluorescence Recovery After Photobleaching (FRAP) and time-lapse imaging

$HeLa^{G3BP1\text{-}EGFP\ OE}$ cells were seeded into an ibidi 18-well plate at a concentration of 5×10^3 cells/well and cultured overnight at 37 °C with 5% CO_2 before being treated with either sodium arsenite (AS), sorbitol, or dye-labeled 60%CLS-AuNPs. Following treatment, cells were washed with pre-warmed D-PBS and moved into a stage-top live imaging chamber (ibidi). FRAP was performed using a laser-scanning Leica inverted microscope with a 100× oil immersion objective with a numerical aperture (NA) equal to 1.47 (Apo oil immersion, Vizla, Germany). At least three stress granules (1–2.5 μm diameter) per condition were selected for photobleaching (10 ms pulse, 30 mW) followed by time-lapse imaging at 2-s intervals. Data normalization and analysis were performed using Leica LAS X software (version 3.2.1).

Analysis of intracellular protein corona

To investigate protein corona adsorbed on nanospheres, HeLa cells were co-cultured with diazirine-modified 60%CLS-AuNPs (50 μL, 10^{12} particles mL^{-1}) for 4 h. Following removal of unbound nanospheres, cells were irradiated with 365 nm ultraviolet light (15 mW/cm^2, 20 min) to facilitate covalent protein-nanosphere crosslinking. Cells were then lysed using RIPA buffer (10 min, PD0013D Beyotime) and centrifuged at 18,000 × *g* to pellet the nanosphere-protein complexes. The resulting precipitate was subjected to chemical etching with KI/I_2 (500 μL, containing 2.5 mM KI and 0.34 mM I_2) to liberate bound proteins, which were subsequently purified through 3 kDa molecular weight cutoff ultrafiltration. Protein identification was performed by label-free LC–MS analysis as described in the following section.

Analysis of extracellular protein trafficking

Magnetic Fe_3O_4 nanoparticles were synthesized via chemical co-precipitation of Fe^{2+} and Fe^{3+} salts under a nitrogen atmosphere, using ammonium hydroxide as the precipitant. The nanoparticles were washed and collected magnetically. Surface amination was achieved by treating the Fe_3O_4 nanoparticles with (3-aminopropyl) triethoxysilane (APTES) under acidic conditions. The resulting aminated nanoparticles (Fe_3O_4-NH_2) were thoroughly washed and dried. For streptavidin conjugation, streptavidin was first activated in PBS using excess EDC and NHS. The activated streptavidin was then reacted with Fe_3O_4-NH_2 nanoparticles. The conjugated beads (Fe_3O_4-Streptavidin) were magnetically separated and blocked with 1% bovine serum albumin (BSA) to minimize non-specific binding.

To analyze the extracellular protein corona, serum proteins were first labeled with tetrazine-sulfo-NHS ester (targeting lysine residues). These tetrazine-labeled proteins were adsorbed onto nanomaterials to form a corona. The corona-coated nanoparticles were isolated, washed, and incubated with cells in wild-type serum. After photoligation and cell lysis, intracellular corona components and total lysate were subjected to click chemistry-mediated immunoprecipitation using a TCO-Biotin linker (RT, 15 min), followed by capture with the prepared Fe_3O_4-Streptavidin magnetic beads. The captured protein corona components were then quantified by Western blotting (WB).

Co-IP experiments and proteomics

The Co-immunoprecipitation (Co-IP) experiment was conducted utilizing the Classic IP Kit (#26146, Thermo Fisher Scientific) to selectively enrich G3BP1 protein along with its interacting partners, in accordance with the manufacturer's instructions. A total of 18 experimental samples were analyzed: three groups (NH_2-AuNPs, 60% CLS-AuNPs, and mPEG-AuNPs, on nanomaterials vs G3BP1-IP alone) × $n = 2$ independent biological replicates each. For each replicate, HeLa cells were treated as described in the main text. The proteomic analysis was conducted by Verygenome Technology Co. Ltd. For the sample preparation, cells were lysed in RIPA buffer (10 min, 4 °C), and nanomaterial–protein complexes were isolated by chemo-etching-assisted proximity labeling (see Fig. 2H). After elution, proteins were reduced with 10 mM DTT (56 °C, 30 min), alkylated with 20 mM iodoacetamide (RT, dark, 30 min), and digested overnight at 37 °C with sequencing-grade trypsin (1:50 enzyme:protein, w/w). Peptides were desalted on C18 StageTips and dried under vacuum prior to LC–MS/MS. Peptides were analyzed on an Easy-nLC 1000 UHPLC coupled to a Q Exactive HF Orbitrap mass spectrometer (Thermo Fisher Scientific). Peptides were separated on a 15 cm × 75 μm ID C18 column (2 μm particle size) using a 90 min linear gradient from 5% to 35% solvent B (0.1% formic acid in acetonitrile) at 300 nL/min. MS acquisition was in data-dependent mode: full MS scans at 60,000 resolution (m/z 350–1,600), AGC target 3e6, max IT 50 ms; top 20 precursors fragmented by HCD (NCE 27), MS/MS resolution 15,000, AGC target 1e5, max IT 100 ms, dynamic exclusion 30 s. Raw files were processed in Proteome Discoverer v2.4 (Thermo) using the Sequest HT search engine against the UniProtKB/Swiss-Prot human database (release 2023_02). Parameters: Enzyme (trypsin, max 2 missed cleavages); Fixed modification (carbamidomethyl, C); Variable modifications (oxidation (M), acetyl (protein N-term)); Precursor mass tolerance (10 ppm); Fragment mass tolerance (0.02 Da); Minimum peptide length (7 amino acids); Peptide-spectrum match (PSM) and protein-level FDR ≤ 1% using Percolator; Minimum 1 unique peptide per protein for identification; Score cut-off: *q*-value < 0.01; PTM localization by ptmRS node (threshold 0.75). Label-free quantification was performed using precursor ion intensities normalized across runs. Statistical analysis of differential protein abundance was conducted in Perseus v1.6.15.0 using log_2-transformed LFQ intensities; missing values were imputed from a normal distribution (width 0.3, downshift 1.8). Significance was assessed by two-sided Student's t-test with Benjamini–Hochberg FDR correction (FDR 0.05). GO and KEGG enrichment were performed using STRING v11.5 and DAVID v6.8. Visualization was done in GraphPad Prism 9 and Cytoscape v3.9.1.

All-atom molecular dynamics simulation

Given that the AuNPs (~70 nm) in the experiment are much larger than those of the hnRNPC and G3BP1 (<10 nm), we modeled the AuNPs using a flat Au(111) substrate with the size of 10.38 × 10.49 nm^2 [50]. mPEG and CLS-PEG with 23 repeat units were used to modify the AuNP surfaces. The three surface-modified AuNPs are composed of 100% mPEG (mPEG), 100% CLS-PEG (100% CLS), and a combination of 40% mPEG and 60% CLS-PEG (60% CLS), respectively. Each PEG molecule is covalently bonded to the AuNP surface via Au-S bonds. The structure of hnRNPC was sourced from AlphaFold (https://alphafold.ebi.ac.uk, UniProt: P07910), while the crystal structure of the NTF2L domain of G3BP1 was obtained from the Protein Data Bank (PDB entry: 7SUO[51]). For the hnRNPC-NTF2L complex, the protein was initially positioned at the center of a cubic box, ensuring that the minimum distance between the protein and its mirror image exceeds 3 nm. The system was solvated in a 12 × 12 × 12 nm^3 cubic box with 53,997 water molecules and 0.15 M NaCl, comprising 169,216 atoms in total. In the case of the AuNPs or the protein-AuNPs complex, the minimum distance between the PEGs or the protein and the mirrored gold substrate is greater than 2 nm. For the protein-AuNPs complex, the protein was initially placed above the AuNPs, with the minimum distance between the protein and the PEGs exceeding 1 nm. Each complex was solvated in water, with NaCl added to neutralize the system at a concentration of 0.15 M. The simulation boxes for the mPEG, 60% CLS, and 100% CLS systems had lateral dimensions of 10.38 × 10.49 nm^2, with z-dimensions of 12.99, 13.48, and 13.49 nm, respectively. Each system contained 4536 Au atoms, 168 PEG molecules, and one hnRNPC protein, solvated with 32,511, 32,304, and 31,002 water molecules, yielding total atom counts of 136,052, 142,713, and 143,631 for the mPEG, 60% CLS, and 100% CLS systems, respectively.

For the hnRNPC-NTF2L complex, the system was first energy-minimized using the steepest descent method until convergence was achieved. This was followed by 500 ps of pre-equilibration in the NVT ensemble and an additional 500 ps in the NPT ensemble, during which all protein heavy atoms were restrained with harmonic potentials of 1000 $kJ{\cdot}mol^{-1}{\cdot}nm^{-2}$. Finally, the restraints were removed, and 500 ns production MD simulations in the NPT ensemble were carried out with a 2 fs timestep. For the AuNP and AuNP-protein systems, after energy minimization, the systems also underwent 500 ps of NVT and 500 ps of NPT pre-equilibration, during which all gold atoms, as well as the heavy atoms of the proteins and PEGs, were restrained with harmonic constraints of 1000 $kJ{\cdot}mol^{-1}{\cdot}nm^{-2}$. Restraints on the proteins and PEGs were subsequently released, followed by 500 ns production simulations in the NPT ensemble with a 2 fs timestep. For each system, we performed three independent simulations to ensure reproducibility. The temperature was maintained at 310 K using the V-rescale thermostat[52] with a time constant of 0.2 ps, while the pressure was

kept at 1 atm using the Parrinello-Rahman barostat with a time constant of 2.0 ps and a compressibility constant of 4.5×10^{-5} bar^{-1}. Notably, in the case of AuNPs or the protein-AuNPs complex, pressure coupling was applied only in the z-direction. The final 200 ns trajectory with an interval of 1 ns from each run was used for binding energy analysis.

All-atom molecular dynamics (MD) simulations were performed using the GROMACS 2020.6 package[53] with the Amber14SB force field[54] and the TIP3P water model. The General Amber force field[55] (GAFF) parameter for mPEG and CLS-PEG, including methoxy and cholesterol, was generated using AmberTools23[56]. RESP2 charge[57] were obtained through B3LYP/def2TZVP quantum calculations of the electrostatic potential, performed with the Gaussian09 program and fitted using Multifwn[58]. Parameters for the gold atom were obtained from previous work[59,60]. The Lennard–Jones interaction was computed using a cutoff of 1.2 nm, and long-range electrostatic interactions were treated using the particle-mesh Ewald (PME) method. The bonds involving hydrogen atoms were constrained by the LINCS algorithm[61]. Periodic boundary conditions were applied in all three directions.

Binding energies were calculated using the molecular mechanics/generalized Born surface area (MM/GBSA) method[62]. The binding energy is composed of four terms, including the van der Waals interaction (ΔE_{VDW}), the electrostatic interaction (ΔE_{ELE}), the polar solvation energy (ΔE_{polar}), and the nonpolar solvation energy (ΔE_{SA}). The contact surface area (CSA) was calculated by

$$CSA = \left(SASA_A + SASA_B - SASA_{AB}\right)/2$$

where SASA represents the solvent accessible surface area, A and B represent the individual molecules, while AB denotes the complex. Typical snapshots and corresponding key residue interface graphs were visualized using PyMOL[63].

NSG microenvironment measurement method

Four distinct HaloTag ligand-dye conjugates were synthesized under light-protected conditions: (1) Protonex Red-HaloTag ligand was prepared by mixing 10 mM Protonex Red and HaloTag ligand solutions in a 1:3-5 molar ratio in PBS buffer at 4 °C overnight (final concentration: 80 μM); (2) LLVY-AMC conjugate was synthesized by combining 10 mM LLVY-AMC, 10 mM HaloTag ligand, and 5 mM acetylene-succinimide in a 2:3:2 molar ratio in PBS buffer with DMSO, followed by 37 °C overnight shaking (final concentration: 1 mM); (3–4) Rhodamine B- and Coumarin-HaloTag ligands were prepared at final concentrations of 14.6 mM and 20 mM, respectively.

For microenvironment imaging, cells were stained with HaloTag ligand-dye conjugates at optimized concentrations: Protonex-HaloTag ligand (0.1 μM), LLVY-HaloTag ligand (1 μM), Rhodamine B-HaloTag ligand (10 nM), and Coumarin-HaloTag ligand (0.1 μM) for 1 h prior to treatment with either sodium arsenite (AS) or 60%CLS-AuNPs, followed by fixation with 4% paraformaldehyde and fluorescence microscopy imaging.

Transcriptome

The transcriptome libraries were prepared using Trizol (R401-01, Vazyme, P.R. China) following the manufacturer's instructions. Transcriptome analysis was provided by Wuhan Frasergen Genomic Medicine CO., Ltd. Raw reads were processed using trim-galore, and clean reads were mapped to mm 10 from UCSC genome1 using Hisat2 (v2.1.0) with default parameters. Differential analysis was performed using edgeR algorithms with fold change ≥1.2 and p-value ≤ 0.05 as the thresholds. For data analysis visualization, the CNSknowall Online Tool (https://cnsknowall.com) was harnessed.

Bio-distribution

Female BALB/C nude mice (4–6 weeks) were purchased from the Comparative Medicine Centre of Yangzhou University and bred at the Specific Pathogen Free (SPF) Experimental Animal Center of Affiliated Nanjing Drum Tower Hospital of Nanjing University Medical School. Mice were housed under a 12-h light/dark cycle at 22–24 °C and 40%–60% humidity with ad libitum access to food and water. Choice of animal sex was made based on the subsequent study, wherein a cervical tumor xenograft was established. For the sample size, it has been specified in each section. Once reaching a body weight of roughly 25 grams, the mice were randomly divided into several groups (detailed treatment as described in each case) post an intravenous injection of CLS-AuNPs (20 mg/Kg body weight) through the tail vein. At certain time points, mice were sacrificed to harvest tissues including liver, spleen, and kidneys. For those tissues, they were weighed, followed by repeated freeze-thawing to entirely release the nanomaterials within cells. Afterwards, the tissues were dissolved in heated aqua regia. DI water was supplemented into the solution to make a final volume of 5 mL containing 1% nitric acid (vol/vol). The content of gold in each sample was measured by using ICP-MS (Agilent 7500ce, Agilent, United States), and the biodistribution profiles of nanomaterials were calculated based on the weight of tissue measured right after collection.

Chemo-toxicity mitigation and chemo-sensitization

To evaluate the action of NSGs formation related to chemo-toxicity mitigation. BALB/c nude mice received a treatment regimen identical to that of the biodistribution assay. After 48 h, the mice received an *i.v.* injection of chemotherapeutic agents through the tail vein (dissolved in saline, 10, 15, and 10 mg/Kg body weight for Doxorubicin, cisplatin, and paclitaxel, respectively). For mice that received only nanomaterials or chemotherapeutics, we followed the same dosage. Peripheral blood of mice was collected, and potential tissue toxicity caused by either nanomaterials or chemotherapeutics was reflected by the measured levels of ALT (Alanine Transaminase), GGT (Gamma-Glutamyl Transferase), and Scr (Serum Creatinine). For β2-MG (β-2-Microglobulin), PDGF (Platelet-derived growth factor), and TNF-α (Tumor necrosis factor α), we harnessed ELISA kits for their measurement (β2-MG: #D721167, Sangon Biotech, P.R. China; PDGF and TNF-α, #KTE4053 and # KTE7015, all from Abbkine, P. R. China).

To evaluate the chemo-toxicity mitigation effect in tumor-bearing mice. The xenograft tumor model was first established using wild-type or gene-edited HeLa cells through subcutaneous injection (4×10^5 cells per mouse) suspended in PBS into the flank of the mouse. According to the ARRIVE guide 2.0[64], mice successfully developed a tumor xenograft were included for subsequent study. After the size of the tumor grew to 100 μm^3, mice were randomly grouped into treated and control groups for subsequent analysis. Animals were randomized into treatment arms using a computer-generated list. Cage distribution was balanced (maximum three animals per cage per treatment). Allocation was concealed by coding treatment syringes/vials; dosing and outcome acquisition were performed by technicians blinded to group labels where feasible. The maximal tumor burden permitted by our IACUC (e.g., 1.5 cm maximal diameter or 1500 mm^3 volume) was not exceeded in any experiment. For the dosage of chemotherapeutics, we followed the treatment regimen as described above, except for nocodazole (5 mg/Kg body weight). For both nanomaterials and chemotherapeutics, they were administered every four days. Mice were sacrificed once their tumor tissue reached a volume of 1 mm^3 or at the end of the therapeutic outcome study. Both the growth curves of the tumor tissue and the overall survival rate of mice in each group were recorded to assess the chem-sensitization action rendered by NSGs.

Protein array assay

Mouse serum was collected and maintained at −80 °C prior to analysis. Antibody array assays (Mouse Inflammation Cytokine Array, Ray

Biotech Inc, United States) were carried out according to the manufacturer's instructions. In brief, the diluted serum was incubated with the microarray glass substrate under gentle shaking, followed by multiple washes to remove unbound cytokines. Afterwards, a cocktail of antibodies and an equivalent amount of dye-conjugated Streptavidin were added stepwise and subjected to repeated washes with PBS. The signals were visualized by using a laser scanner equipped with a filter for the corresponding dye (Axon GenePix). Data was extracted using ScanArray Express.

Flow-cytometry analysis

For the quantification of the viability of cancer cells, mice in different groups were sacrificed at 8 h post-treatment, with their tumor tissues harvested and cleaned rapidly through ice-cold PBS to remove blood and tissue debris. Afterwards, the tumor tissue was minced into pieces with a mean volume of 2-5 mm^3 using an eye scissor. These tissue fragments were immediately transferred to DMEM/F12 culture medium (Gibco) supplemented with 30 μg of type IV collagenase (Sigma–Aldrich) and type I DNase (Roche) and incubated for 4 h at 37 °C under gentle shaking. The softened tumor tissue was next filtered through a 400-mesh screen, followed by centrifugation (200 × *g* for 5 min). Cell debris in the supernatant was discarded, and the cells were resuspended with PBS for labeling with Annexin V-FITC/PI (#KGA108, Keygen Biotech., P.R. China) following the manufacturer's instructions. Flow-cytometry analysis was conducted on FACS Verse (BD Bioscience, United States) and processed using FlowJo software (version 10.0.7).

Statistical analysis

All experiments were repeated $n = 3$ independent biological replicates unless stated otherwise. The unit of analysis for statistics was the per-replicate mean to avoid inflating n with technical repeats. Data are shown as mean ± SD (unless box/violin plots are used, for which center, box, and whiskers respectively mean median, IQR, and 5th–95th percentiles; all data points were displayed unless their presentation prevents the plot from being clearly visualized, in this case, the entire information can be found in the source data). Statistical tests are stated in each legend; two-sided tests were used with Tukey correction for multiple comparisons after one-way ANOVA (normality met) or Kruskal–Wallis otherwise. *P*-values, test statistics (t/F/df), and sample sizes can be found in legends or Source Data. No data were excluded unless pre-specified (see "Reporting summary" section).

No formal statistical power calculation was performed prior to this study because effect sizes for nanomaterial-induced stress granule formation and related in vivo outcomes were not available in the literature. Instead, sample sizes were based on (i) prior studies of stress granules and nanomaterials reporting robust effect sizes with $n = 3$ biological replicates for cell-based assays and $n = 5$–7 animals per group for xenograft models, and (ii) Nature Portfolio's minimum standards for reproducibility. For cell-based experiments, each condition was repeated in ≥3 independent biological replicates on different days, analyzing ≥200 randomly selected cells per-replicate; the unit of analysis was the per-replicate mean. For animal studies, group sizes ($n = 5$ for toxicity assays; $n = 7$ for therapeutic outcome trials) were chosen to allow detection of large effect sizes observed in pilot experiments while minimizing animal use, consistent with ARRIVE guidelines. Baseline tumor volume and body weight were balanced across groups to reduce variability. These sample sizes yielded consistent results across replicates, and raw data are provided in the Source Data file.

Reporting summary

Further information on research design is available in the Nature Portfolio Reporting Summary linked to this article.

Data availability

Unless otherwise stated, all data supporting the results of this study are available in the article, Supplementary Information, and Source Data files. RNA-seq data are deposited under NCBI BioProject under accession code PRJNA1311971 [https://dataview.ncbi.nlm.nih.gov/object/PRJNA1294231?reviewer=lnradfp6uv0tsh0df2o7g09foa]. Proteomics data have been deposited to PRIDE/ProteomeXchange under accession code PXD067940 [https://www.iprox.cn/page/subproject.html?id=IPX0013238001]. Source Data are provided with this paper.

Code availability

All-atom simulations code is available on the FigShare Project repository [https://doi.org/10.6084/m9.figshare.29995738].

References

1. Banani, S. F., Lee, H. O., Hyman, A. A. & Rosen, M. K. Biomolecular condensates: organizers of cellular biochemistry. *Nat. Rev. Mol. Cell Biol.* **18**, 285–298 (2017).
2. Anderson, P. & Kedersha, N. Stress granules. *Curr. Biol.* **19**, R397–R398 (2009).
3. Protter, D. S. W. & Parker, R. Principles and properties of stress granules. *Trends Cell Biol.* **26**, 668–679 (2016).
4. Guillén-Boixet, J. et al. RNA-induced conformational switching and clustering of G3BP drive stress granule assembly by condensation. *Cell* **181**, 346–361 (2020).
5. Yang, P. et al. G3BP1 is a tunable switch that triggers phase separation to assemble stress granules. *Cell* **181**, 325–345 (2020).
6. Hu, S. et al. Time-resolved proteomic profiling reveals compositional and functional transitions across the stress granule life cycle. *Nat. Commun.* **14**, 7782 (2023).
7. Leśniczak-Staszak, M. et al. Stress granule-mediated sequestration of EGR1 mRNAs correlates with lomustine-induced cell death prevention. *J. Cell Sci.* **137**, jcs261825 (2024).
8. Dong, T. et al. G3BP1/2-targeting PROTAC disrupts stress granules dependent ATF4 migracytosis as cancer therapy. *J. Am. Chem. Soc.* **147**, 446–461 (2025).
9. Li, X. et al. Stress granules sequester autophagy proteins to facilitate plant recovery from heat stress. *Nat. Commun.* **15**, 10910 (2024).
10. Li, H. et al. MG53 suppresses tumor progression and stress granule formation by modulating G3BP2 activity in non-small cell lung cancer. *Mol. Cancer* **20**, 118 (2021).
11. Mehta, S. & Zhang, J. Liquid-liquid phase separation drives cellular function and dysfunction in cancer. *Nat. Rev. Cancer* **22**, 239–252 (2022).
12. Li, T., Zeng, Z., Fan, C. & Xiong, W. Role of stress granules in tumorigenesis and cancer therapy. *Biochim. Biophys. Acta Rev. Cancer* **1878**, 189006 (2023).
13. Ryan, V. H. & Fawzi, N. L. Physiological, pathological, and targetable membraneless organelles in neurons. *Trends Neurosci.* **42**, 693–708 (2019).
14. Yang, X., Yang, M., Pang, B., Vara, M. & Xia, Y. Gold nanomaterialas at work in biomedicine. *Chem. Rev.* **115**, 10410–10488 (2015).
15. Sperling, R., Gil, P., Zhang, F., Zanella, M. & Parak, W. Biological applications of gold nanoparticles. *Chem. Soc. Rev.* **37**, 1896–1908 (2008).
16. Liu, J. et al. Emerging of ultrafine membraneless organelles as the missing piece of nanostress: mechanism of biogenesis and implications at multilevels. *ACS Nano* **19**, 5659–5679 (2025).
17. Zheng, Y. et al. Seed-mediated synthesis of single-crystal gold nanospheres with controlled diameters in the range 5-30 nm and their self-assembly upon dilution. *Chem. Asian J.* **8**, 792–799 (2013).
18. Li, Q. et al. Decoding the interplay between m^6A modification and stress granule stability by live-cell imaging. *Sci. Adv.* **10**, eadp5689 (2024).

19. Fu, Y. & Zhuang, X. m^6A-binding YTHDF proteins promote stress granule formation. *Nat. Chem. Biol.* **16**, 955–963 (2020).
20. Gasset-Rosa, F. et al. Cytoplasmic TDP-43 de-mixing independent of stress granules drives inhibition of nuclear import, loss of nuclear TDP-43, and cell death. *Neuron* **102**, 339–357 (2019).
21. Han, S. et al. Endosomal sorting results in a selective separation of the protein corona from nanoparticles. *Nat. Commun.* **14**, 295 (2023).
22. Liu, S. et al. Mammalian IRE1α dynamically and functionally coalesces with stress granules. *Nat. Cell Biol.* **26**, 917–931 (2024).
23. Zheng, W. et al. C9orf72 regulates the unfolded protein response and stress granule formation by interacting with eIF2α. *Theranostics* **12**, 7289–7306 (2022).
24. Chen, Z. et al. Screening membraneless organelle participants with machine-learning models that integrate multimodal features. *Proc. Natl. Acad. Sci. USA* **119**, e2115369119 (2022).
25. Kozakov, D. et al. The ClusPro web server for protein-protein docking. *Nat. Protoc.* **12**, 255–278 (2017).
26. Abramson, J. et al. Addendum: accurate structure prediction of biomolecular interactions with AlphaFold 3. *Nature* **636**, E4 (2024).
27. Song, D. et al. Yin and yang regulation of stress granules by Caprin-1. *Proc. Natl. Acad. Sci. USA* **119**, e2207975119 (2022).
28. Zhao, Z. et al. QKI shuttles internal m^7G-modified transcripts into stress granules and modulates mRNA metabolism. *Cell* **186**, 3208–3226 (2023).
29. Ren, J. et al. Emerging implications of phase separation in cancer. *Adv. Sci.* **9**, e2202855 (2022).
30. Los, G. V. et al. HaloTag: a novel protein labeling technology for cell imaging and protein analysis. *ACS Chem. Biol.* **3**, 373–382 (2008).
31. Soleilhac, A. et al. Temperature response of rhodamine B-doped latex particles: from solution to single particles. *Langmuir* **32**, 4052–4058 (2016).
32. Salehian, F. et al. A review: biologically active 3,4-heterocycle-fused coumarins. *Eur. J. Med. Chem.* **212**, 113034 (2021).
33. Ye, S. et al. Micropolarity governs the structural organization of biomolecular condensates. *Nat. Chem. Biol.* **20**, 443–451 (2024).
34. Shin, Y. & Brangwynne, C. P. Liquid phase condensation in cell physiology and disease. *Science* **357**, eaaf4382 (2017).
35. Riback, J. A. et al. Composition-dependent thermodynamics of intracellular phase separation. *Nature* **581**, 209–214 (2020).
36. Gwon, Y. et al. Ubiquitination of G3BP1 mediates stress granule disassembly in a context-specific manner. *Science* **372**, eabf6548 (2021).
37. Sahu, I. et al. The 20S as a stand-alone proteasome in cells can degrade the ubiquitin tag. *Nat. Commun.* **12**, 6173 (2021).
38. Böddeker, T. J. et al. Non-specific adhesive forces between filaments and membraneless organelles. *Nat. Phys.* **18**, 571–578 (2022).
39. Klein, I. A. et al. Partitioning of cancer therapeutics in nuclear condensates. *Science* **368**, 1386–1392 (2020).
40. Liz-Marzán, L. M. et al. What do we mean when we say nanomedicine? *ACS Nano* **16**, 13257–13259 (2022).
41. de Lázaro, I. & Mooney, D. J. Obstacles and opportunities in a forward vision for cancer nanomedicine. *Nat. Mater.* **20**, 1469–1479 (2021).
42. Monopoli, M. P. et al. Biomolecular coronas provide the biological identity of nanosized materials. *Nat. Nanotechnol.* **7**, 779–786 (2012).
43. Lu, X. et al. Tailoring the component of protein corona via simple chemistry. *Nat. Commun.* **10**, 4520 (2019).
44. Cong, Y. et al. Protein corona-mediated inhibition of nanozyme activity: Impact of protein shape. *J. Am. Chem. Soc.* **146**, 10478–10488 (2024).
45. Portz, B., Lee, B. L. & Shorter, J. FUS and TDP-43 phases in health and disease. *Trends Biochem. Sci.* **46**, 550–563 (2021).
46. Boyko, S. & Surewicz, W. K. Tau liquid-liquid phase separation in neurodegenerative diseases. *Trends Cell Biol.* **32**, 611–623 (2022).
47. Dahiya, V. et al. The switch from client holding to folding in the Hsp70/Hsp90 chaperone machineries is regulated by a direct interplay between co-chaperones. *Mol. Cell* **82**, 1543–1556 (2022).
48. Andrikopoulos, N. et al. Exploring peptido-nanocomposites in the context of amyloid diseases. *Angew. Chem. Int. Ed.* **63**, e202309958 (2023).
49. Ko, T. W. et al. A fourth-generation high-dimensional neural network potential with accurate electrostatics including non-local charge transfer. *Nat. Commun.* **12**, 398 (2021).
50. Mokashi-Punekar, S., Walsh, T. R. & Rosi, N. L. Tuning the structure and chiroptical properties of gold nanoparticle single helices via peptide sequence variation. *J. Am. Chem. Soc.* **141**, 15710–15716 (2019).
51. Biswal, M., Lu, J. & Song, J. SARS-CoV-2 nucleocapsid protein targets a conserved surface groove of the NTF2-like domain of G3BP1. *J. Mol. Biol.* **434**, 167516 (2022).
52. Bussi, G., Donadio, D. & Parrinello, M. Canonical sampling through velocity rescaling. *J. Chem. Phys.* **126**, 014101 (2007).
53. Abraham, M. J. et al. GROMACS: High performance molecular simulations through multi-level parallelism from laptops to supercomputers. *SoftwareX* **1**, 19–25 (2015).
54. Maier, J. A. et al. ff14SB: Improving the accuracy of protein side chain and backbone parameters from ff99SB. *J. Chem. Theory Comput.* **11**, 3696–3713 (2015).
55. Wang, J. et al. Development and testing of a general amber force field. *J. Comput. Chem.* **25**, 1157–1174 (2004).
56. Case, D. A. et al. AmberTools. *J. Chem. Inf. Model.* **63**, 6183–6191 (2023).
57. Schauperl, M. et al. Non-bonded force field model with advanced restrained electrostatic potential charges (RESP2). *Commun. Chem.* **3**, 44 (2020).
58. Lu, T. & Chen, F. Multiwfn: a multifunctional wavefunction analyzer. *J. Comput. Chem.* **33**, 580–592 (2012).
59. Heinz, H., Vaia, R., Farmer, B. & Naik, R. Accurate simulation of surfaces and interfaces of face-centered cubic metals using 12-6 and 9-6 Lennard-Jones potentials. *J. Phys. Chem. C.* **112**, 17281–17290 (2008).
60. Rai, B. et al. Molecular dynamic simulations of self-assembled alkylthiolate monolayers on an Au(III) surface. *Langmuir* **20**, 3138–3144 (2004).
61. Hess, B. P-LINCS: A parallel linear constraint solver for molecular simulation. *J. Chem. Theory Comput.* **4**, 116–122 (2008).
62. Valdés-Tresanco, M. S. et al. gmx_MMPBSA: a new tool to perform end-state free energy calculations with GROMACS. *J. Chem. Theory Comput.* **17**, 6281–6291 (2021).
63. DeLano, W. L. PyMOL: an open-source molecular graphics tool. *CCP4 Newsl. Protein Crystallogr.* **40**, 82–92 (2002).
64. Percie du Sert, N. et al. The ARRIVE guidelines 2.0: updated guidelines for reporting animal research. *PLoS Biol.* **18**, e3000410 (2020).

Acknowledgements

This work was supported by the National Natural Science Foundation of China (12347102, 32371447, 12222506, and 82473182), Jiangsu Provincial Outstanding Youth Fund (BK20230001), and Jiangsu Province "333" project (No. (2022) 3-1-234).

Author contributions

L.Z., Z.Y., and X.L. contributed equally. Conceptualization: L.Z., H.D., Q.L., Y.M., and D.H. raised the idea of investigating nanomaterials' potential to modulate biomolecular condense. Methodology: L.Z. and D.H. developed the chemo-etching-assisted proximity labeling method and

synthetic strategy. Investigation: L.Z. performed wet-chemical synthesis, fluorescence imaging, and preparation of a sample for Omics studies. Z.Y. conducted a molecular dynamics simulation. X.L. aided in micro-environment imaging analysis. J.C. and X.T. contributed partially to the bioinformatic analysis. Q.L. conducted the animal studies.; Data visualization: L.Z. contributed to the preparation of all figures appearing in both the main text and supplementary materials with the help of Y.W.; Writing-original draft: L.Z. and Z.Y. drafted the manuscript, which was revised by H.D. and D.H.; Supervision: H.D., Q.L., Y.M., and D.H. supervised the study.

Competing interests
The authors declare no competing interests.

Additional information
Supplementary information The online version contains supplementary material available at https://doi.org/10.1038/s41467-025-64623-4.

Correspondence and requests for materials should be addressed to Hong-Ming Ding, Qin Liu, Yu-Qiang Ma or Da Huo.

Peer review information *Nature Communications* thanks Pu Chun Ke, Ole Jakob Nøstbakken, and the other anonymous reviewer(s) for their contribution to the peer review of this work. A peer review file is available.